



A charge-sensing region in the stromal interaction molecule 1 luminal domain confers stabilization-mediated inhibition of SOCE in response to S-nitrosylation

Received for publication, October 18, 2017, and in revised form, March 29, 2018. Published, Papers in Press, April 16, 2018, DOI 10.1074/jbc.RA117.000503

Jinhui Zhu, Xiangru Lu, Qingping Feng¹, and Peter B. Stathopoulos²

From the Department of Physiology and Pharmacology, University of Western Ontario, London, Ontario N6A 5C1, Canada

Edited by Roger J. Colbran

Store-operated Ca²⁺ entry (SOCE) is a major Ca²⁺ signaling pathway facilitating extracellular Ca²⁺ influx in response to the initial release of intracellular endo/sarcoplasmic reticulum (ER/SR) Ca²⁺ stores. Stromal interaction molecule 1 (STIM1) is the Ca²⁺ sensor that activates SOCE following ER/SR Ca²⁺ depletion. The EF-hand and the adjacent sterile α -motif (EFSAM) domains of STIM1 are essential for detecting changes in luminal Ca²⁺ concentrations. Low ER Ca²⁺ levels trigger STIM1 destabilization and oligomerization, culminating in the opening of Orai1-composed Ca²⁺ channels on the plasma membrane. NO-mediated S-nitrosylation of cysteine thiols regulates myriad protein functions, but its effects on the structural mechanisms that regulate SOCE are unclear. Here, we demonstrate that S-nitrosylation of Cys⁴⁹ and Cys⁵⁶ in STIM1 enhances the thermodynamic stability of its luminal domain, resulting in suppressed hydrophobic exposure and diminished Ca²⁺ depletion-dependent oligomerization. Using solution NMR spectroscopy, we pinpointed a structural mechanism for STIM1 stabilization driven by complementary charge interactions between an electropositive patch on the core EFSAM domain and the S-nitrosylated nonconserved region of STIM1. Finally, using live cells, we found that the enhanced luminal domain stability conferred by either Cys⁴⁹ and Cys⁵⁶ S-nitrosylation or incorporation of negatively charged residues into the EFSAM electropositive patch in the full-length STIM1 context significantly suppresses SOCE. Collectively, our results suggest that S-nitrosylation of STIM1 inhibits SOCE by interacting with an electropositive patch on the EFSAM core, which modulates the thermodynamic stability of the STIM1 luminal domain.

Ca²⁺ ions are universal signaling entities regulating countless processes including programmed cell death, homeostasis, gene transcription, and muscle contraction (1). To closely regulate these processes, Ca²⁺ is compartmentalized with a low

cytosolic concentration (~0.0001 mM) compared with a high extracellular concentration (~1 mM) when cells are at rest (2). Moreover, intracellular organelles such as the endoplasmic reticulum (ER)³ contain a relatively high Ca²⁺ concentration (~0.4–0.7 mM) that can be released into the cytosol in response to electrical or chemical stimuli (3, 4). Remarkably, emptying of ER Ca²⁺ stores can mobilize Ca²⁺ entry from the extracellular space in a ubiquitous process termed store operated Ca²⁺ entry (SOCE) (5). Upon sarcoplasmic reticulum (SR) or ER Ca²⁺ depletion, stromal interaction molecule 1 (STIM1), which is inserted in the ER/SR membrane becomes oligomerized, translocates to ER–plasma membrane junctions and interacts with Orai1 (6–11), facilitating the formation and opening of Orai1-composed Ca²⁺ release-activated Ca²⁺ (CRAC) channels (12–16). Open CRAC channels enable Ca²⁺ to move down the steep concentration gradient from the extracellular space into the cytosol. The movement of extracellular Ca²⁺ into the cytosol replenishes the depleted stores and drives myriad signaling processes that require sustained cytosolic Ca²⁺ elevation such as the immune response (4).

The cytosolic domains of STIM proteins contain a series of coiled-coil domains that contribute to oligomerization and are required for coupling to and gating of Orai1 channels (17–22). However, the luminal domains of STIM proteins contain the essential ER/SR Ca²⁺ sensing machinery, which initiate SOCE after ER/SR Ca²⁺ store depletion (10, 23, 24). The luminal domain of STIMs are made up of highly conserved canonical EF-hand (residues 63–96) and noncanonical EF-hand (residues 97–128) motifs adjacent to a similarly well conserved sterile α -motif (SAM) domain (residues 132–200) that make up the EFSAM core and mediate the Ca²⁺ sensing function (Fig. 1A). The noncanonical EF-hand is hydrogen-bonded with the canonical EF-hand, forming a pocket for interactions with the SAM domain in the presence of Ca²⁺ (24). When the canonical EF-hand loses Ca²⁺, the protein undergoes a partial unfolding-

This work was supported by Natural Sciences and Engineering Research Council of Canada Grant 05239 (to P. B. S.), Canadian Foundation for Innovation/Ontario Research Fund Grant 34113 (to P. B. S.), and Canadian Institutes of Health Research Grant MOP-142383 (to Q. F.). The authors declare that they have no conflicts of interest with the contents of this article.

This article contains Table S1 and Figs. S1–S6.

¹ To whom correspondence may be addressed: Dept. of Physiology and Pharmacology, University of Western Ontario, 1151 Richmond St. N, London, ON N6A 5C1, Canada. E-mail: qingping.feng@schulich.uwo.ca.

² To whom correspondence may be addressed: Dept. of Physiology and Pharmacology, University of Western Ontario, 1151 Richmond St. N, London, ON N6A 5C1, Canada. E-mail: peter.stathopoulos@schulich.uwo.ca.

³ The abbreviations used are: ER, endoplasmic reticulum; SR, sarcoplasmic reticulum; SOCE, store-operated Ca²⁺ entry; STIM1, stromal interaction molecule 1; SAM, sterile α -motif; EFSAM, EF-hand together with the adjacent SAM; CRAC, Ca²⁺ release-activated Ca²⁺; ANS, 8-anilino-1-naphthalene-1-sulfonic acid; DLS, dynamic light scattering; HSQC, heteronuclear single quantum coherence; PRE, paramagnetic relaxation enhancement; MTSL, 1-oxyl-2,2,5,5-tetramethyl- Δ 3-pyrroline-3-methyl methanethiosulfonate; mChSTIM1, monomeric cherry-tagged STIM1; TG, thapsigargin; DiBAC₄(3), bis-(1,3-dibutylbarbituric acid)-trimethine oxonol; TIRF, total internal reflective fluorescence; GSNO, S-nitrosoglutathione; HBSS, HEPES-buffered saline solution.

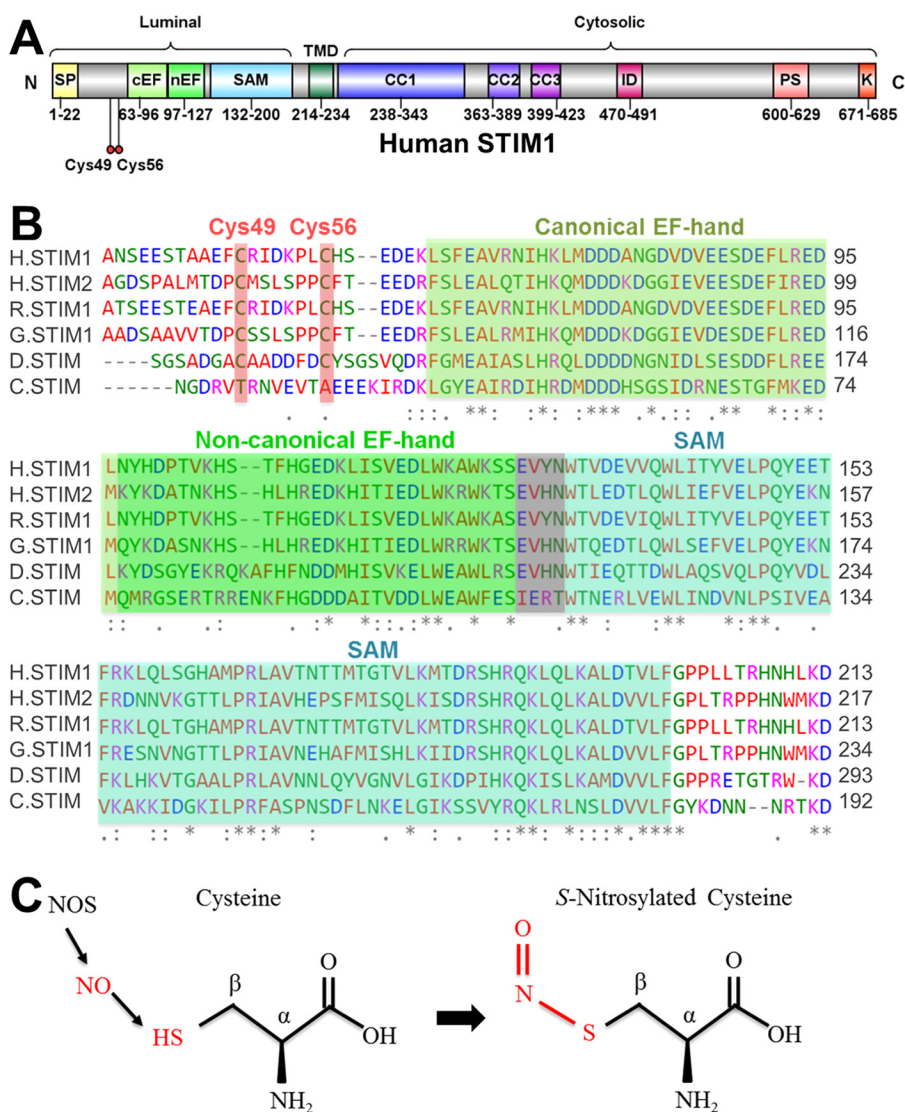


Figure 1. Domain architecture and primary sequence alignment of STIMs. A, STIM1 domain architecture. The locations of the signal peptide (SP, yellow), two luminal Cys residues (red spheres), canonical EF-hand (cEF, light green), noncanonical EF-hand (nEF, green), SAM domain (cyan), transmembrane domain (TMD, dark green), three coiled-coil segments (CC1, blue; CC2, purple; CC3, violet), inhibitory domain (ID, magenta), serine/proline-rich region (PS, pink), and lysine-rich region (K, red) are shown relative to the N and C termini. Residue ranges are shown below each domain. B, alignment of luminal STIM primary sequences. *Homosapiens* STIM1 (H.STIM1, NCBI accession NP_003147.2), *Homosapiens* STIM2 (H.STIM2, NCBI accession NP_065911.3), *Rattus norvegicus* STIM1 (R.STIM1, NCBI accession NP_001101966.2), *Gallus gallus* STIM1 (G.STIM1, NCBI accession XP_420749.5), *Drosophila melanogaster* STIM (D.STIM, NCBI accession NP_523357.2), and *Caenorhabditis elegans* STIM (C.STIM, NCBI accession CCD73857.1) sequences were aligned in Clustal Omega (70). Fully conserved (*), highly conserved (:), and partially conserved (.) positions are shown below the respective residue. The conserved Cys⁴⁹ and Cys⁵⁶ positions are shaded red. C, depiction of the mechanism through which cysteine residues are S-nitrosylated. The atoms directly modified via S-nitrosylation are highlighted in red.

induced destabilization, coupled with oligomerization, which is the initiation event for SOCE activation (10, 24, 25). Chimeric STIM with the luminal domains replaced by FK506-binding protein can induce SOCE in response to rapamycin treatment, which pharmacologically oligomerizes FK506-binding protein, totally independent of ER luminal Ca²⁺ (23), reinforcing the criticality of STIM1 luminal domain oligomerization to SOCE initiation.

The short, nonconserved N-terminal regions of human STIM1 and STIM2 can modulate the stability of the Ca²⁺-sensing EFSAM core and the activation of SOCE (25, 26). Further, there are two cysteine residues (i.e. Cys⁴⁹ and Cys⁵⁶ in STIM1) that are conserved among vertebrate and some lower order STIM homologues (Fig. 1B). STIM1 Cys⁵⁶ can undergo S-glutathionylation following oxidative stress, which results in con-

stitutively activated SOCE, independent of luminal Ca²⁺ levels (27). Given this susceptibility to oxidative stress and other proteases found to be both S-glutathionylated and S-nitrosylated (28, 29), these Cys residues are also candidate sites for S-nitrosylation. S-Nitrosylation is a readily reversible Cys modification that may occur in the presence of an NO donor and an electron acceptor. Specifically, S-nitrosylation involves the addition of NO groups onto reduced Cys residues to form S-nitrosocysteines (Fig. 1C). S-Nitrosylation of Cys residues can affect protein stability, activation, structure, localization, and function (30).

Here, we used high excess NO donor availability to study the effects of STIM1 S-nitrosylation on the Ca²⁺-sensing mechanism and Orai1 activation. Using biophysical and biochemical approaches, we found that S-nitrosylation of Cys⁴⁹ and Cys⁵⁶

S-Nitrosylation inhibits STIM1 via charge sensing by EFSAM

enhances the thermodynamic stability, suppresses the surface-exposed hydrophobicity, and deoligomerizes the STIM1 luminal domain. Further, we identified an electropositive interaction site on the core EFSAM domain by solution NMR spectroscopy, which mediates stabilization through interactions with the Cys-containing nonconserved region. Remarkably, incorporation of negative charges into this patch by mutation increases the thermodynamic stability, independent of NO availability. Finally, we demonstrate in live HEK293 cells co-expressing full-length STIM1 and Orai1 that stabilization of the STIM1 luminal domain using NO donors or via mutation of the electropositive patch suppresses SOCE. Collectively, our experiments uncover a charge-sensing region in the core EFSAM domain that confers stabilization in response to *S*-nitrosylation and endows STIM1 with an additional layer of regulation.

Results

S-Nitrosylation induces thermodynamic stabilization of STIM1 23–213

SOCE is initiated after Ca^{2+} -depletion-dependent destabilization of the EFSAM core leads to oligomerization and STIM1 puncta formation (10, 11, 31, 32). The nonconserved, N-terminal region of STIM1 contains two Cys residues and plays a role in modulating the stability of the EFSAM core (25). Given the importance of EFSAM stability to SOCE activation, we performed a precise quantification of the thermodynamic stability of the entire STIM1 luminal domain (*i.e.* residues 23–213) using equilibrium chemical denaturation curves in the presence and absence of Ca^{2+} and *S*-nitroglutathione (GSNO). The urea denaturation process was completely reversible and, thus, amenable to two-state equilibrium unfolding analysis. The Gibbs free energy of unfolding in water ($\Delta G_{\text{H}_2\text{O}}$), denaturant dependence of the unfolding transition (*m* value), and the midpoint of urea denaturation (C_{mid}) were extracted from the urea denaturation curves using the linear extrapolation method (33). The Ca^{2+} -loaded STIM1 luminal domain revealed a $\Delta G_{\text{H}_2\text{O}}$ of $5.9 \text{ kcal mol}^{-1}$ in the presence of 1 mM DTT (*i.e.* reduced state). After *S*-nitrosylation of the Ca^{2+} -loaded protein by ultrafiltration into a buffer containing 1 mM GSNO and no reducing agent, we observed an increase in the $\Delta G_{\text{H}_2\text{O}}$ by $+2.0 \text{ kcal mol}^{-1}$ (Fig. 2, A and B, and Table S1). We observed a similar GSNO-dependent enhancement of $\Delta G_{\text{H}_2\text{O}}$ by $+1.5 \text{ kcal mol}^{-1}$ under the Ca^{2+} -depleted conditions (Fig. 2, C and D, and Table S1).

To probe whether the sensitivity to the presence of GSNO was facilitated by the Cys⁴⁹ and Cys⁵⁶ residues, we generated C49S/C56S to prevent *S*-nitrosylation at these sites. We focused on Ca^{2+} -depleted equilibrium denaturation because this state is the SOCE initiation-competent state. The Ca^{2+} -depleted C49S/C56S protein exhibited a similar $\Delta G_{\text{H}_2\text{O}}$ as the WT; however, whereas GSNO robustly enhanced the stability of the WT form, the double Cys mutant showed no enhancement of stability in the presence of the NO donor (Fig. 2, E and F, and Table S1). Thus, GSNO thermodynamically stabilizes the STIM1 luminal domain in a Cys⁴⁹- and Cys⁵⁶-specific manner.

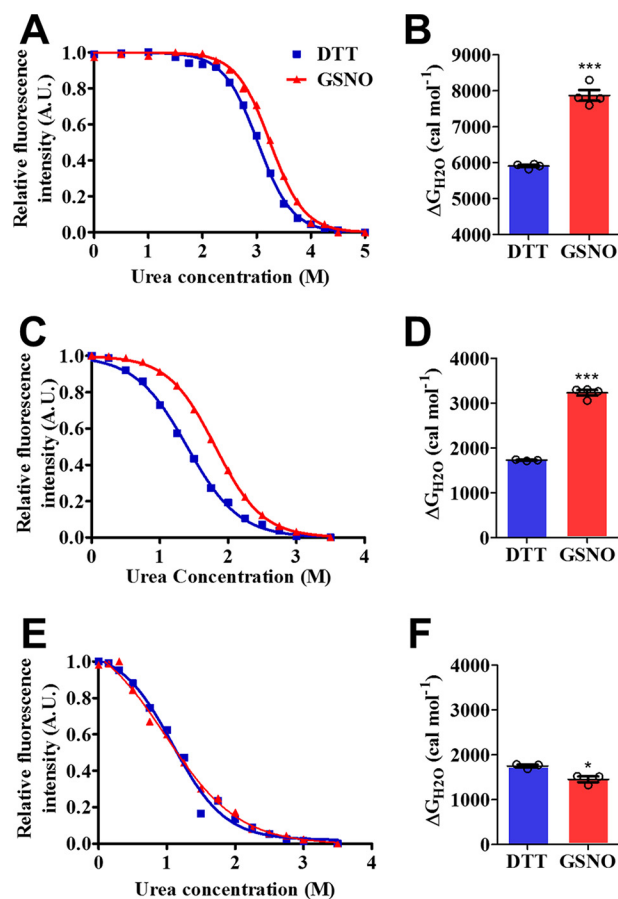


Figure 2. Equilibrium chemical denaturation curves of STIM1 23–213. A, representative urea denaturation curves of Ca^{2+} -loaded WT STIM1 23–213. B, $\Delta G_{\text{H}_2\text{O}}$ comparison of the Ca^{2+} -loaded WT STIM1 23–213 in the presence of 1 mM DTT or 1 mM GSNO. C, representative urea denaturation curves of Ca^{2+} -depleted WT STIM1 23–213. D, $\Delta G_{\text{H}_2\text{O}}$ comparison of Ca^{2+} -depleted WT STIM1 23–213 in the presence of 1 mM DTT or 1 mM GSNO. E, representative urea denaturation curves of Ca^{2+} -depleted C49S/C56S STIM1 23–213. F, $\Delta G_{\text{H}_2\text{O}}$ comparison of Ca^{2+} -depleted C49S/C56S STIM1 23–213 in the presence of 1 mM DTT or 1 mM GSNO. In A, C, and E, the solid blue and red lines represent the two-state unfolding model fit to the data for the DTT- and GSNO-treated samples, respectively. In B, D, and F, the data are means \pm S.E. of $n = 3$ separate experiments. *, $p < 0.05$; ***, $p < 0.0001$.

S-Nitrosylation decreases the level of solvent-exposed STIM1 23–213 hydrophobicity

The Ca^{2+} -depletion-induced oligomerization of STIM1 EFSAM is associated with increased solvent-accessible hydrophobicity (10). Thus, we next sought to evaluate the level of exposed STIM1 23–213 hydrophobicity in the presence and absence of the NO donor using the extrinsic fluorescence probe 8-anilino-1-naphthalene-sulfonic acid (ANS), which becomes hyperfluorescent when bound to exposed hydrophobic patches of proteins (34). The fluorescence emission of ANS was enhanced >2 -fold in the presence of the Ca^{2+} -depleted WT STIM1 23–213; however, the addition of excess CaCl_2 markedly decreased the ANS fluorescence indicative of Ca^{2+} -binding induced folding (Fig. 3A). In contrast, the ANS fluorescence was only marginally increased when incubated with Ca^{2+} -depleted WT STIM1 23–213 in the presence of 1 mM GSNO compared with the buffer alone; further, the addition of excess CaCl_2 resulted in only a minimal change in the ANS fluorescence intensity (Fig. 3B). To confirm that the differences in

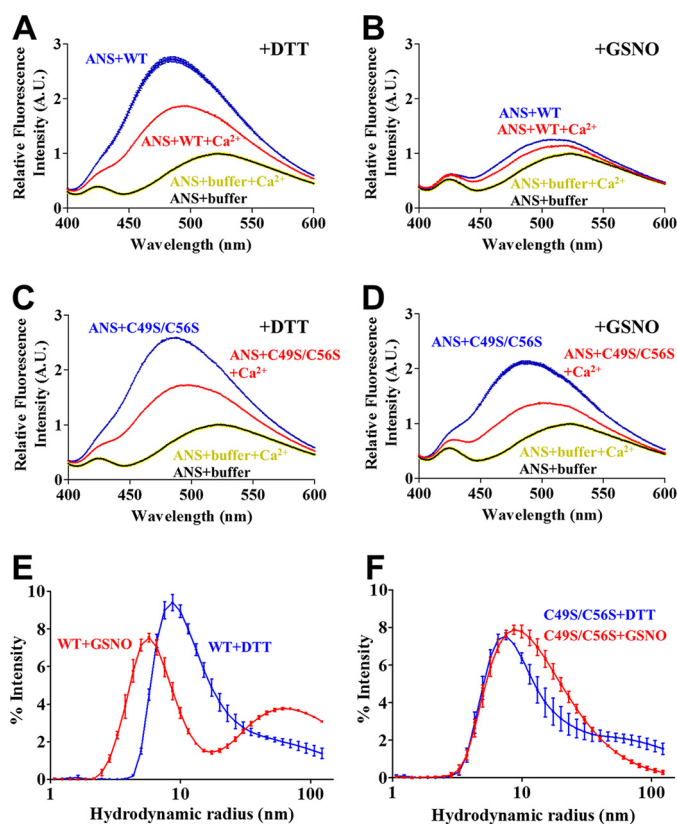


Figure 3. Surface hydrophobicity levels and oligomerization assessment of STIM1 23–213. A, relative change in ANS fluorescence intensity of WT STIM1 23–213 in DTT buffer. B, relative change in ANS fluorescence intensity of WT STIM1 23–213 in GSNO buffer. C, relative change in ANS fluorescence intensity of C49S/C56S STIM1 23–213 in DTT buffer. D, relative change in ANS fluorescence intensity of C49S/C56S STIM1 23–213 in GSNO buffer. In A–D, ANS fluorescence emission spectra are shown for buffer (black), buffer plus Ca²⁺ (yellow), protein (blue), and protein plus Ca²⁺ (red) samples. E, regularization deconvolution of the distribution of hydrodynamic radii from the autocorrelation functions of Ca²⁺-depleted WT STIM1 23–213 in the presence of DTT (blue traces) and GSNO (red traces). F, regularization deconvolution of the distribution of hydrodynamic radii from the autocorrelation functions of Ca²⁺-depleted C49S/C56S STIM1 23–213 in the presence of DTT (blue traces) and GSNO (red traces). The data in A–F are means ± S.E. of *n* = 3 separate experiments.

ANS binding were caused by alterations in protein folding, we monitored the relative change in intrinsic fluorescence upon Ca²⁺ binding in the presence and absence of GSNO. Indeed, we observed a <2% compared with >20% maximal change in intrinsic fluorescence during Ca²⁺ titration experiments in the presence and absence of 1 mM GSNO, respectively (Fig. S1), indicating that the NO donor induces a conformation with suppressed Ca²⁺-binding-induced structural allostery.

Next, we repeated the ANS-binding experiments using the C49S/C56S STIM1 23–213 protein to probe the role of the Cys residues in the GSNO responses. The C49S/C56S protein showed a >2-fold increase in the ANS fluorescence that was markedly suppressed by the addition of excess CaCl₂ (Fig. 3C). Importantly, the C49S/C56S STIM1 23–213 protein exhibited a similar >2-fold increase in ANS fluorescence even in the presence of 1 mM GSNO; moreover, the addition of 5 mM CaCl₂ suppressed this ANS fluorescence, consistent with the Ca²⁺-binding induced folding (Fig. 3D). Collectively, the ANS data demonstrate that Ca²⁺ binding or GSNO treatment suppresses solvent exposed hydrophobicity of STIM1 23–213 and that the

effect of the NO donor depends on the presence of the Cys⁴⁹ and Cys⁵⁶ thiols.

STIM1 23–213 undergoes *S*-nitrosylation-mediated deoligomerization

To test whether the effects of *S*-nitrosylation on stability, hydrophobicity, and structure correlate with oligomerization propensity, we next assessed hydrodynamic size of STIM1 23–213 by dynamic light scattering (DLS). Because the Ca²⁺-loaded state of STIM1 23–213 is a monomer (10, 24, 25), we focused on the oligomerized Ca²⁺-depleted protein. Regularization deconvolution of the size distributions from the autocorrelation functions showed that exchange of Ca²⁺-depleted STIM1 23–213 from DTT-containing buffer to 1 mM GSNO-containing buffer systematically decreased the smallest distribution of hydrodynamic radii (Fig. 3E). Although the change in hydrodynamic size distribution appears modest, the difference is, in fact, marked given that light scattering intensity scales with particle size to the sixth power (35). Thus, the hydrodynamic sizes <7 nm contribute >95% of the light scattering signal in the GSNO-treated sample. On the other hand, the STIM1 23–213 C49S/C56S double mutant protein did not undergo deoligomerization after being exchanged into the GSNO (Fig. 3F). Taken together, the DLS observations demonstrate that GSNO deoligomerizes luminal STIM1 in a Cys⁴⁹- and Cys⁵⁶-dependent manner, consistent with the suppressed hydrophobicity and the enhanced stability observed for the *S*-nitrosylated and Ca²⁺-depleted protein.

The nonconserved STIM1 24–57 region interacts with EFSAM Trp121 and Lys122

Although the atomic-resolution structure of the STIM1 EFSAM core has been solved by solution NMR spectroscopy (24), the structure of the full STIM1 23–213 luminal domain remains unresolved. Thus, to probe where the Cys⁴⁹ and Cys⁵⁶ residues may interact with EFSAM, we applied a solution NMR spectroscopy approach. Titration of unlabeled STIM1 24–57 peptide both in the presence and absence of GSNO into a solution of uniformly ¹⁵N-labeled STIM1 EFSAM did not affect the ¹H-¹⁵N HSQC EFSAM spectrum, indicating that interactions (if any) between these regions are relatively weak. To further probe the possibility of weak/transient interactions, we tagged the STIM1 24–57 peptide with a nitroxide spin label via the Cys⁴⁹ and Cys⁵⁶ thiols. Interactions between the nitroxide spin-labeled Cys⁴⁹ and/or Cys⁵⁶ residues and the ¹⁵N-labeled STIM1 EFSAM would cause paramagnetic relaxation enhancement (PRE) of atom resonances within ~10 Å of the tags (36), causing peak broadening and reduced peak intensity. Because the nitroxide tagging is mediated by an 1-oxyl-2,2,5,5-tetramethyl-Δ3-pyrroline-3-methyl methanethiosulfonate (MTSL) functional group, reducing agents such as DTT can remove the covalent disulfide linkage and provide a baseline spectrum with no PRE effects for comparison. First, we checked the efficiency of our PRE protocol by nitroxide tagging the Cys residues in uniformly ¹⁵N-labeled STIM1 24–57 and acquiring a ¹H-¹⁵N HSQC spectrum. Most of the cross-peaks in the ¹H-¹⁵N correlation spectrum of the peptide were severely broadened, consistent with efficient labeling of the peptide; moreover, addition

S-Nitrosylation inhibits STIM1 via charge sensing by EFSAM

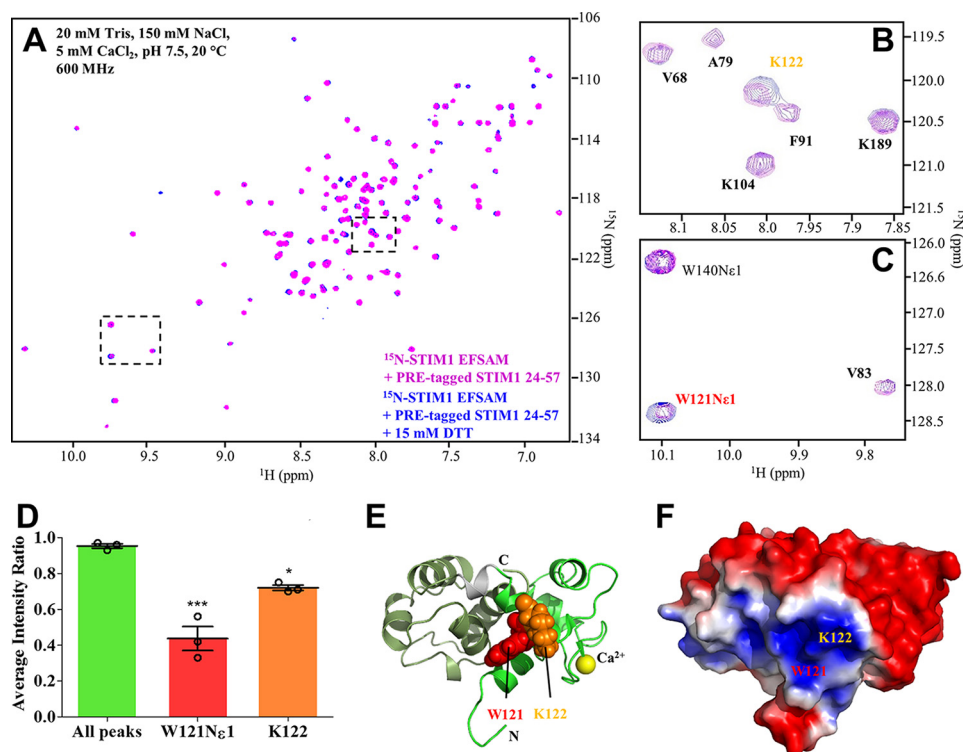


Figure 4. NMR assessment of interactions between STIM1 24–57 and EFSAM. *A*, representative ^1H - ^{15}N HSQC spectra of STIM1 EFSAM mixed with nitroxide spin-labeled STIM1 24–57 before (*magenta*) and after the addition of 15 mM DTT (*blue*). *Dashed boxes* bound regions where cross-peaks underwent a reproducible intensity broadening. *B*, zoomed view of the Lys 122 amide N(H) cross-peak showing a loss in peak intensity. *C*, zoomed view of the Trp 121 side chain N(H) cross-peak showing a loss in peak intensity. Residue assignments in *B* and *C* are shown beside the respective cross-peak with the Trp 121 and Lys 122 labels indicated in *red* and *orange*, respectively. *D*, average intensity ratio of all cross-peaks relative to the Trp 121 side chain and Lys 122 backbone N(H) ratios. *E*, ribbon representation of the Ca^{2+} -loaded STIM1 EFSAM structure. The EF-hand (*light green*) and SAM domain (*dark green*) are connected by a short linker region (*gray*). The interaction site between the STIM1 24–57 peptide and the EF-hand domain is localized near the W121Ne1 (*red spacefill*) and Lys 122 (*orange spacefill*) residues. The Ca^{2+} atom is shown as a *yellow sphere*. *F*, electrostatic surface potential of Ca^{2+} -loaded STIM1 EFSAM. The surface potential is shown as a gradient between +2 and –2 kT/e determined using the APBS and PDB2PQR tools (71, 72). The locations of the Trp 121 and Lys 122 residues relative to the distinct electropositive patch are shown. The data in *C* are means \pm S.E. of $n = 3$ separate experiments. The structure images in *E* and *F* were rendered in PyMOL (PyMOL Molecular Graphics System, version 1.7; Schrödinger). *, $p < 0.05$; ***, $p < 0.0001$.

of 15 mM DTT to the sample restored the intensity of all the cross-peaks, confirming our modification and reversal procedure (Fig. S2).

Next, we mixed unlabeled, but nitroxide-tagged STIM1 24–57 with uniformly ^{15}N -labeled EFSAM and acquired a ^1H - ^{15}N HSQC spectrum in the absence and presence of 15 mM DTT. The vast majority of EFSAM cross-peaks were unaffected by the 24–57 peptide (Fig. 4A); however, the side chain Trp 121 indole N(H) and backbone amide Lys 122 N(H) cross-peaks were reproducibly broadened compared with the same cross-peaks in spectra obtained after the addition of 15 mM DTT (Fig. 4, B and C). Consistently, the average intensity ratio (*i.e.* absence/presence of DTT) of all N(H) cross-peaks for the protein mixture was close to 1, whereas the broadening effect caused by the nitroxide spin labels resulted in a significantly lower intensity ratio for the EFSAM Trp 121 and Lys 122 signals (Fig. 4D).

Mapping these residue positions on the three-dimensional solution structure of the Ca^{2+} -loaded STIM1 EFSAM core shows that these two residues are located in the EF-hand domain, spatially near the N-terminal end of EFSAM where the unresolved STIM1 24–57 region would hypothetically extend (Fig. 4E). Plotting the electrostatic potential on the surface of EFSAM reveals that these residues contribute to the formation of a distinctly electropositive surface patch on EFSAM (Fig. 4F),

which is complementary to the electronegative potential of *S*-nitrosylated Cys 49 and Cys 56 (37). Taken together, our solution NMR data suggest that the Cys 49 and/or Cys 56 of the STIM1 24–57 region complementarily interact(s) with the EFSAM core at a distinctly electropositive patch on the surface of the EF-hand domain.

W121E/K122E-mediated electrostatic surface charge reversal enhances the stability and supersedes the structural effects of GSNO on STIM1 23–213

To probe the role of the identified electropositive region in interceding the structure and stability sensitivity to *S*-nitrosylation, we generated a W121E/K122E double mutant in the STIM1 23–213 context. We expected that either (i) this mutant would inhibit the *S*-nitrosylation-mediated effects by charge repulsion or (ii) the mutant would mimic the effect *S*-nitrosylation by disruption of the electropositive continuity on the EFSAM surface (Fig. S3). We first assessed the thermodynamic stability of Ca^{2+} -depleted W121E/K122E STIM1 23–213 in the presence and absence of GSNO using urea denaturation experiments. Remarkably, the $\Delta G_{\text{H}_2\text{O}}$ of the W121E/K122E protein was +2.2 kcal mol $^{-1}$ higher than the WT protein, even in the absence of the NO donor; moreover, GSNO increased the $\Delta G_{\text{H}_2\text{O}}$ by +0.4 kcal mol $^{-1}$, much less than the +1.5 kcal

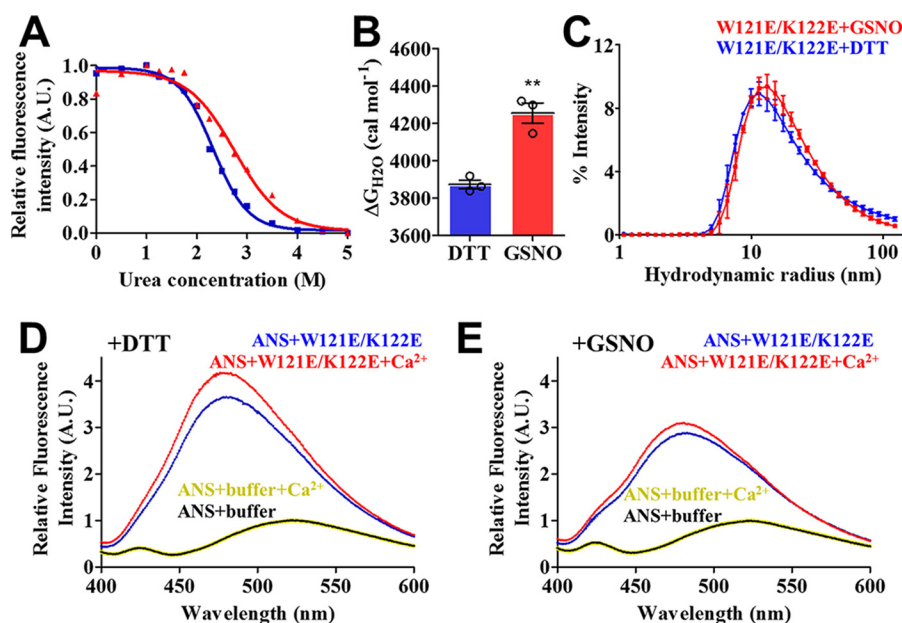


Figure 5. Biophysical characterization of W121E/W122E STIM1 23–213. *A*, representative urea denaturation curves of Ca^{2+} -depleted W121E/W122E STIM1 23–213. The solid blue and red lines represent the two-state unfolding model fit to the data for the DTT and GSNO-treated protein, respectively. *B*, $\Delta G_{\text{H}_2\text{O}}$ comparison of the Ca^{2+} -depleted W121E/W122E STIM1 23–213 in the presence of 1 mM DTT or 1 mM GSNO. *C*, regularization deconvolution of the distribution of hydrodynamic radii from the autocorrelation functions of Ca^{2+} -depleted W121E/W122E STIM1 23–213 in the presence of DTT (blue traces) and GSNO (red traces). *D*, relative change in ANS fluorescence intensity of W121E/W122E STIM1 23–213 in DTT buffer. *E*, relative change in ANS fluorescence intensity of W121E/W122E STIM1 23–213 in GSNO buffer. In *D* and *E*, ANS fluorescence emission spectra are shown for buffer (black), buffer plus Ca^{2+} (yellow), protein (blue), and protein plus Ca^{2+} (red) samples. The data in *A–E* are means \pm S.E. of $n = 3$ separate experiments. **, $p < 0.001$.

mol^{-1} observed with the WT protein (Fig. 5, *A* and *B*, and Table S1). Next, we evaluated the ability of GSNO to deoligomerize W121E/K122E STIM1 23–213 by DLS. The distribution of hydrodynamic radii was unaffected by the addition of GSNO (Fig. 5*C*), in contrast to the WT protein, which underwent a distinct shift in the distribution to smaller hydrodynamic radii in the presence of the NO donor (Fig. 3*E*). Finally, we investigated how the surface hydrophobicity of W121E/K122E STIM1 23–213 responded to Ca^{2+} and GSNO using ANS-binding experiments. In the absence of GSNO, W121E/K122E STIM1 23–213 enhanced the ANS fluorescence by >3 -fold, indicating considerable surface-exposed hydrophobicity; however, upon addition of excess Ca^{2+} , the ANS fluorescence remained high, suggesting a minimal structural change upon Ca^{2+} binding (Fig. 5*D*). The presence of the GSNO donor only minimally affected these ANS spectra, which showed an ~ 3 -fold increase in fluorescence both with and without excess Ca^{2+} (Fig. 5*E*). Collectively, these data demonstrate that incorporation of negative charges into the electropositive EFSAM patch by mutation thermodynamically stabilizes STIM1 23–213 and desensitizes both oligomerization and changes in surface hydrophobic exposure (with and without Ca^{2+}) to GSNO treatment.

S-Nitrosylation of Cys⁴⁹ and Cys⁵⁶ or W121E/K122E inhibits STIM1-mediated SOCE in live cells

Having observed a Cys⁴⁹- and Cys⁵⁶-dependent thermodynamic stabilization of the isolated STIM1 luminal domain in response to GSNO treatment concomitant with deoligomerization and suppressed exposed hydrophobicity, we investigated whether this structure and stability sensitivity is linked to the regulation of full-length STIM1 function in live mammalian

cells. We used Fura-2 ratiometric Ca^{2+} fluorimetry to probe SOCE in HEK293 cells stably expressing YFP-Orai1 and overexpressing monomeric cherry-tagged STIM1 (mChSTIM1). SOCE was induced in these cells after thapsigargin (TG) blockade of the sarco/endoplasmic reticulum Ca^{2+} ATPase pumps passively depleted the ER Ca^{2+} stores, and 2 mM net CaCl_2 was added back to the extracellular medium. As expected, the cells transfected with WT mChSTIM1 showed significantly higher levels of SOCE gauged from the maximal change in the Fura-2 fluorescence ratio following Ca^{2+} addback compared with empty mCherry vector transfected or untransfected controls; moreover, overnight incubation of the WT mChSTIM1-expressing cells with GSNO significantly decreased the maximal level of Ca^{2+} uptake after the Ca^{2+} addition (Fig. 6, *A* and *B*). To test whether the suppressed SOCE caused by the GSNO was driven by the STIM1 Cys⁴⁹ and Cys⁵⁶ residues of the nonconserved domain, we expressed the full-length C49S/C56S mChSTIM1 protein in the HEK293 cells and reassessed SOCE. Indeed, the maximal level of Ca^{2+} uptake in cells expressing this double Cys mutant version of mChSTIM1 was similar to the WT protein in the absence of GSNO and was unaffected by GSNO incubation (Fig. 6, *A* and *B*).

Given that the W121E/K122E STIM1 23–213 luminal domain protein showed an enhanced thermodynamic stability and a much lesser stabilization after GSNO treatment compared with WT, we anticipated that cells expressing this W121E/K122E mutant would exhibit suppressed SOCE even in the absence of the NO donor. As expected, we found that cells expressing full-length W121E/K122E STIM1 showed a significantly reduced maximal Ca^{2+} uptake compared with the WT protein. Overnight treatment of the W121E/K122E-expressing

S-Nitrosylation inhibits STIM1 via charge sensing by EFSAM

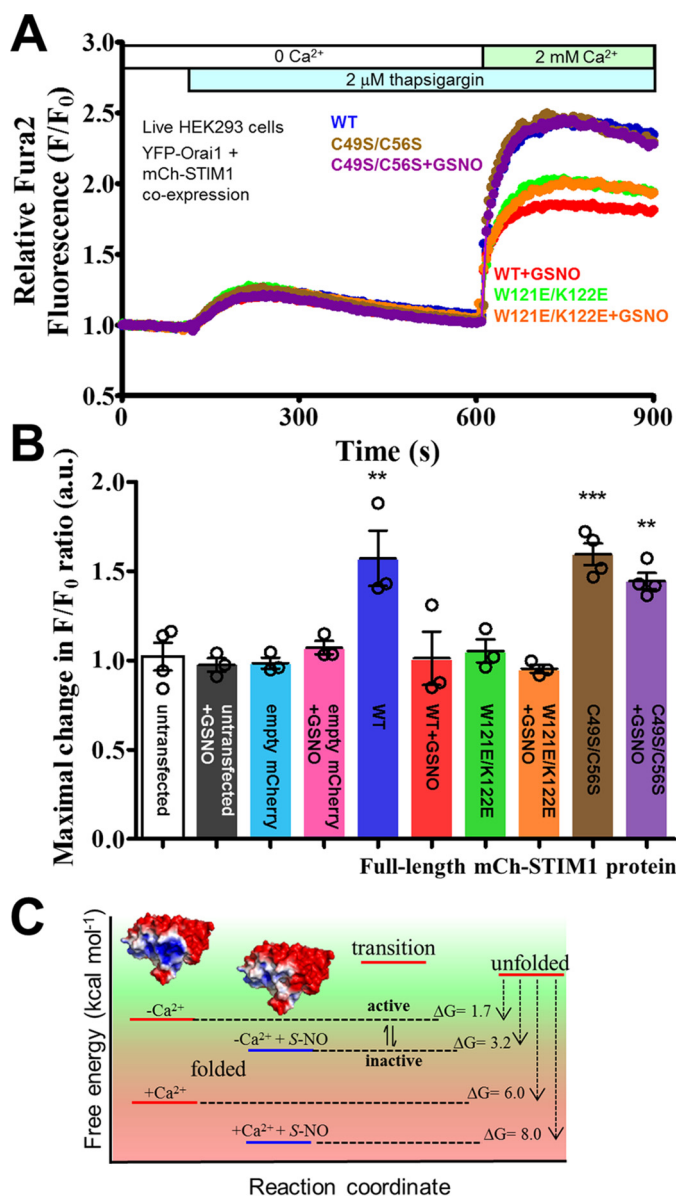


Figure 6. GSNO sensitivity of SOCE in live HEK293 cells expressing full-length Orai1 and STIM1. *A*, representative Fura-2 ratiometric fluorescence traces reporting on relative changes in cytosolic Ca²⁺ levels. The cells were initially bathed in Ca²⁺-free buffer. The relative change in Fura-2 fluorescence was monitored after 2 μM TG and subsequently 2 mM Ca²⁺ additions to the external medium. *B*, maximal relative change in Fura-2 signal after the 2 mM Ca²⁺ addition indicative of level of SOCE. In *A* and *B*, WT STIM1 data are colored blue and red, W121E/K122E STIM1 data are colored green and orange, and C49S/C56S STIM1 data are colored brown and purple for cells incubated in the absence and presence of GSNO, respectively. In *B*, the data are means ± S.E. of *n* = 3–4 separate experiments. ***, *p* < 0.001; **, *p* < 0.01 versus empty mCherry. *C*, relative stability scheme of the luminal Ca²⁺ sensing region of STIM1. The scheme depicts the relative energies of the active and inactive conformation highlighting the relatively smaller threshold required to inhibit STIM1 activation upon S-nitrosylation compared with the stabilization which occurs upon Ca²⁺ binding.

cells with GSNO did not affect the level of SOCE any further (Fig. 6, *A* and *B*).

To ensure that GSNO incubation did not alter protein expression levels or membrane potential of our HEK293 cells and to confirm that GSNO affects STIM1 activation, we performed Western blotting, bis-(1,3-dibutylbarbituric acid)-trimethine oxonol (DiBAC₄(3)) fluorimetry, and live cell total

internal reflective fluorescence (TIRF) imaging, respectively. Our Western blots showed no significant differences in mCh-STIM1 WT or mutant protein expression levels in our HEK293 cells with or without GSNO, consistent with total mCh-STIM1 and YFP-Orai1 fluorescence assessments (Fig. S4). Further, the depolarization-induced DiBAC₄(3) fluorescence changes were not affected by GSNO in these cells (Fig. S5). Consistent with our Fura-2 data, TIRF imaging of HeLa cells demonstrated a suppressed ability of WT mCh-STIM1 to form TG-induced puncta when treated with GSNO, whereas the C49S/C56S mCh-STIM1 readily formed TG-induced puncta even in the presence of GSNO, and the W121E/K122E mCh-STIM1 protein exhibited constitutively inhibited puncta formation (Fig. S6).

Collectively, these live cell experiments show that GSNO suppresses STIM1-mediated STIM1 activation and SOCE in a Cys⁴⁹- and Cys⁵⁶-dependent manner, consistent with the thermodynamic stabilization of the isolated luminal domain caused by the NO donor; moreover, incorporation of negative charges into the electropositive EFSAM surface patch, which interacts with the Cys⁴⁹ and/or Cys⁵⁶ residues inhibits SOCE, independent of GSNO treatment. We likely did not observe a GSNO-mediated effect in untransfected and empty mCherry vector-transfected cells because SOCE was already repressed by the stable overexpression of YFP-Orai1 (38).

Discussion

We found that incubation of STIM1 23–213 with excess GSNO thermodynamically stabilizes this domain via a mechanism which involves enhanced folding mediated through interactions between Cys⁴⁹ and/or Cys⁵⁶ located in the nonconserved 24–57 region and an electropositive surface patch on EFSAM. The structural change facilitated by this interaction suppresses both surface-exposed hydrophobicity and oligomerization, which drive STIM1 initiation of SOCE (10, 23, 24). Several lines of evidence suggest that S-nitrosylation of Cys⁴⁹ and Cys⁵⁶ is the principal modification in our experiments. First, numerous studies have demonstrated S-nitrosylation of proteins using an excess NO donor treatment strategy (39–42). Second, S-glutathionylation, a possible modification with the use of GSNO, destabilizes the STIM1 luminal domain and promotes STIM1-mediated activation of SOCE, an effect opposite to the S-nitrosylation-mediated inhibition of SOCE observed herein (see below) (27). Third, incubation with weak NO donors such as S-nitroso-N-acetyl-DL-penicillamine or low concentrations of sodium nitroprusside does not alter STIM1 23–213 stability. Finally, the C_β of both Cys⁴⁹ and Cys⁵⁶ are markedly shifted downfield in NMR spectra, consistent with modification at the S_γ atom.

S-Nitrosyl groups can be readily transferred from GSNO to free thiols in a process termed trans-nitrosylation (43–45). Trans-glutathionylation is a much slower reaction, commonly observed after oxidative bursts (46). Indeed, Hawkins *et al.* (27) utilized hydrogen peroxide to induce STIM1 S-glutathionylation. We did not include a similar oxidative burst in our incubation, thereby favoring S-nitrosylation. Nevertheless, S-nitrosyl groups can be exchanged for GSH (44, 46). Ultimately, the preference for each modification is determined by the local solvent environment, local protein structure, and stability asso-

ciated with the modification. Because *S*-nitrosylation stabilizes the STIM1 23–213, whereas *S*-glutathionylation destabilizes the domain via reduced Ca²⁺-binding affinity (10, 27), we now know that the *S*-nitrosylated conformation is thermodynamically favored in our system of GSNO incubation.

S-Nitrosylated proteins often affect the structure and function of downstream binding partners, thereby transducing regulatory effects relatively distant from the modification site (30, 47, 48). Dysregulated *S*-nitrosylation or denitrosylation can result in serious pathological conditions. For instance, the metabolic enzyme GSNO reductase can selectively reduce the *S*-nitrosyl group from GSNO or cellular proteins and is tightly regulated to maintain physiological homeostasis and prevent nitrosative stress-induced damage (49).

The region of STIM proteins N-terminal to the core EFSAM domain can greatly influence EFSAM stability and the activation kinetics of Orai1 channels (25, 26). Although these far N-terminal regions are highly variable among species, the two Cys residues (*i.e.* Cys⁴⁹ and Cys⁵⁶ in human STIM1) are conserved among vertebrates and many lower order eukaryotic STIM proteins. This evolutionary conservation is evidence for the important role of these Cys residues in SOCE regulation. Indeed, it has been shown that oxidative stress can lead to *S*-glutathionylation of Cys⁵⁶; moreover, this reversible modification decreases the Ca²⁺ binding to the EF-hand domain and induces STIM1 oligomerization and constitutive Ca²⁺ entry (27). Although *S*-glutathionylation and *S*-nitrosylation have competing effects on SOCE (*i.e.* activating *versus* inhibiting, respectively), it is remarkable that the structural mechanism converges on a common target: the EF-hand domain. In the case of *S*-glutathionylation, the EF-hand domain unbinds Ca²⁺ in a structural mechanism that has yet to be elucidated, whereas in the case of *S*-nitrosylation, interactions with the electropositive patch on the EF-hand domain stabilizes EFSAM and inhibits activation. Disulfide formation of Cys⁴⁹ and Cys⁵⁶ has also been suggested to effect STIM1 activation, where the ER oxidoreductase Erp57 interacts with Cys⁴⁹ and Cys⁵⁶ in the ER lumen and inhibits SOCE (50). Thus, the Cys residues in the nonconserved luminal region of STIM proteins function as both oxidative and nitrosative sensors that regulate the function of STIM proteins dependent on the local environment in the ER lumen.

Other studies have described both protein stabilizing (51–55) and destabilizing effects (56–58) of *S*-nitrosylation; hence, the role of this post-translational modification in folding and stability appears to be protein specific. For example, *S*-nitrosylation of ubiquitin C-terminal hydrolase L1 at residues Cys⁹⁰, Cys¹⁵², and Cys²²⁰ decreases its structural stability, promotes aggregation, and catalyzes the oligomerization of α -synuclein which forms Lewy bodies in Parkinson's patients (56). On the other hand, *S*-nitrosylation of surfactant protein-D promotes the formation of smaller species in lieu of the dodecamers or higher order multimers (59). More recently, *S*-nitrosylation of the rhodanese domain from the *Escherichia coli* YgaP protein at Cys⁶³ was found to enhance the stability of the α 4 helix and concomitantly cause a structural alteration in the active site (60), congruent with the similar stabilization/structural changes we observed herein for STIM1. Nevertheless, here we

have quantified the thermodynamic stability changes (*i.e.* ΔG_{H_2O}) associated with *S*-nitrosylation, providing the first insights, to our knowledge, on how the folded to unfolded equilibrium of proteins can be regulated by NO.

The ER luminal region of STIM1 becomes activated under Ca²⁺-depleted conditions after adopting a destabilized conformation that triggers self-association (10); moreover, this oligomerization is the initiation event that drives transmembrane domain reorientation (61), followed by cytosolic coiled-coil domain extension (19, 62), higher order homotypic coiled-coil assembly (18, 22), and the coupling with Orai1 subunits (17, 20, 21) that opens the CRAC channels. We discovered that an electropositive patch on the EFSAM domain senses the *S*-nitrosylation and promotes stabilization of the luminal domain, thereby preventing this series of events. Remarkably, adding negative charges into the positive patch stabilizes the domain, independent of GSNO. Intriguingly, although the oligomerization of W121E/K122E STIM1 23–213 is insensitive to GSNO treatment, the distribution of hydrodynamic radii are persistently high rather than low as would be expected by enhanced stability (63). Thus, the stabilized conformation adopted by the W121E/K122E protein must be distinct from the Ca²⁺-loaded conformation of the WT protein. Consistent with this notion, Ca²⁺ binding to the W121E/K122E protein does not reduce the exposed hydrophobicity as observed for the WT protein. We speculate that the stabilized W121E/K122E conformation represents an intermediate inactive state between the active and inactive conformations.

In conclusion, our data reveal that *S*-nitrosylation-mediated thermodynamic stabilization of the luminal STIM1 23–213 region by +1.5 kcal mol⁻¹ is sufficient to inhibit SOCE activation even in the absence of Ca²⁺; moreover, this stabilization is associated with a suppression of exposed hydrophobicity, which leads to deoligomerization of the luminal protein (Fig. 6C). The stabilization is driven by complementary interactions between electronegative Cys-NO groups and an electropositive patch on the core EFSAM domain, an effect that can be mimicked by mutational introduction of negative charges in the same region. Given that Ca²⁺-binding-induced stabilization of the luminal domain is +4.3 kcal mol⁻¹, the *S*-nitrosylation-mediated +1.5 kcal mol⁻¹ increase represents a lower stabilization threshold to SOCE inhibition. Hence, other luminal domain modifications or even biomolecular interaction events that more moderately modulate protein stability than Ca²⁺ binding will have the potential to regulate SOCE.

Materials and methods

Generation and recombinant expression of STIM1 constructs

The luminal region of *Homo sapiens* STIM1 (NCBI accession NP_003147.2) corresponding to residues 23–213 was cloned into a pET-28a vector (Novagen) using NheI and XhoI restriction sites and expressed with an N-terminal His₆ tag. The *H. sapiens* STIM1 residues 24–57 was subcloned into the pGEX-4T1 (GE Healthcare) vector using BamHI and EcoRI restriction sites and expressed as a GSH-*S*-transferase fusion. A Tyr residue was introduced by site-directed mutagenesis immediately N-terminal to residue 24 to enhance protein detection via Co-

S-Nitrosylation inhibits STIM1 via charge sensing by EFSAM

massie staining and facilitate UV at 280 nm protein concentration measurements. This Tyr mutant and the C49S/C56S and W121E/K122E mutants were introduced into the respective vectors using the QuikChange PCR-based protocol (Agilent).

The His₆-STIM1 23–213 WT, C49S/C56S, and W121E/K122E mutant proteins were expressed in BL21(DE3) codon plus *E. coli* cells and purified under denaturing conditions as described in the nickel-nitrilotriacetic acid agarose beads manufacturer protocol (HisPur; Thermo Fisher Scientific). Refolding was performed by overnight dialysis in ~65 volumes of 20 mM Tris-HCl, 300 mM NaCl, 1 mM DTT, 5 mM CaCl₂, pH 8. The His₆ tags were removed by overnight incubation with ~2 units of bovine thrombin (Calbiochem) per mg of protein. Size-exclusion chromatography through a Superdex 200 10/300 GL (GE Healthcare) was performed as the final purification step. The His₆-STIM1 EFSAM domain was expressed and purified as previously described (10, 64). The pGEX-4T1 STIM1 Y-24–57 was expressed in BL21(DE3) codon plus *E. coli* cells and purified according to GSH-S-transferase–Sephacryl beads manufacturer protocol (Genscript). The STIM1 Y-24–57 peptide was liberated from the beads by overnight thrombin digestion (~5 units/mg of protein) in 20 mM Tris-HCl, 150 mM NaCl, 1 mM DTT, pH 7.5. Size-exclusion chromatography through the Superdex 200 10/300 GL column was performed as the final purification step.

The protein concentrations of STIM1 Y-24–57, STIM1 23–213, STIM1 C49S/C56S-23–213, STIM1 W121E/K122E-23–213, and STIM1-EFSAM were estimated using $\epsilon_{280\text{ nm}} = 0.3296, 1.2418, 1.2436, 0.9909, \text{ and } 1.6062 \text{ (mg ml}^{-1}\text{)}^{-1} \text{ cm}^{-1}$ extinction coefficients.

Ca²⁺ depletion and S-nitrosylation of STIM1

Ca²⁺-depleted STIM1 proteins were prepared by overnight incubation in 50 mM EDTA followed by 20 × 20 × 20-fold exchange by ultrafiltration into nominally Ca²⁺-free buffer. GSNO was prepared as previously described (65). The concentration of GSNO was estimated using $\epsilon_{335\text{ nm}} = 0.92 \text{ mM}^{-1} \text{ cm}^{-1}$ (43). Proteins were exchanged into a buffer containing high excess NO donor (*i.e.* 1 mM GSNO) by ultrafiltration using a 20 × 20 × 20-fold total buffer exchange.

Urea equilibrium denaturation curves

Protein samples diluted to 5 μM were incubated overnight at 25 °C in the presence of 0–5 M urea. Intrinsic fluorescence measurements were taken for each sample using an excitation wavelength (λ_{ex}) = 280 nm and emission wavelength (λ_{em}) = 339 or 337 nm for the Ca²⁺-loaded and Ca²⁺-depleted conditions, respectively, on a temperature-equilibrated Cary Eclipse spectrofluorimeter (Varian/Agilent). Thermodynamic stability parameters (*i.e.* Gibbs free energy of unfolding in the absence of denaturant ($\Delta G_{\text{H}_2\text{O}}$), denaturant dependence of ΔG (m value) and the C_{mid}) were extracted from the chemical denaturation curves according to a two-state unfolding model using the linear extrapolation method (33).

ANS fluorescence

Extrinsic ANS (Sigma) fluorescence was assessed on the Cary Eclipse spectrofluorimeter using 0.14 mg ml⁻¹ protein and 0.05

mM ANS for each experiment. The extrinsic ANS-induced fluorescence emission spectrum was acquired from 400 to 600 nm using a $\lambda_{\text{ex}} = 372 \text{ nm}$ at 37 °C.

Ca²⁺ binding affinity

Changes in intrinsic fluorescence at 37 °C as a function of increasing Ca²⁺ concentration were used to indirectly estimate Ca²⁺-binding affinity. Fluorescence emission spectra between 300 and 450 nm were acquired on a Cary Eclipse spectrofluorimeter using 0.1 mg ml⁻¹ protein and $\lambda_{\text{ex}} = 280 \text{ nm}$. The equilibrium dissociation constant (K_d) was estimated using a one site-binding model, which takes into account protein concentration.

DLS analysis

DLS measurements were made on a DynaPro Nanostar (Wyatt) at 37 °C. Protein samples at 0.46 mg ml⁻¹ were centrifuged at 12,000 × *g* for 10 min before a 5-μl aliquot of the supernatant was loaded into a JC501 microcuvette (Wyatt). The sample was equilibrated for 5 min before 10 consecutive acquisitions were recorded with each acquisition averaged for 5 s. The autocorrelation function was deconvoluted with the regularization algorithm in the accompanying Dynamics software (Wyatt) to extract the distribution of hydrodynamic radii for each sample.

NMR spectroscopy

For nitroxide spin-labeling, the STIM1 Y-24–57 protein was exchanged into 20 mM MOPS, 50 mM NaCl, and 0.1 mM tris(2-carboxyethyl)phosphine-HCl, pH 8.3. Subsequently, MTSL was added to the peptide solution at a final concentration of 4 mM, and the sample was incubated in the dark at ambient temperature for 2 h. Finally, the nitroxide spin-labeled peptide was dialyzed into 20 mM Tris-HCl, 50 mM NaCl, and 5 mM CaCl₂, pH 7.4.

¹H-¹⁵N HSQC spectra (66, 67) were acquired on a 600 MHz Inova NMR spectrometer (Varian/Agilent) using a 5,000 Hz ¹H sweep width, 1,700 Hz ¹⁵N sweep width, 16 transients, and 64 increments in the ¹⁵N dimension for the STIM1 Y-24–57 peptide and 8,000 Hz ¹H sweep width, 1,800 Hz ¹⁵N sweep width, 32 transients, and 64 increments in the ¹⁵N dimension for EFSAM. All NMR samples contained 60 μM 4,4-dimethyl-4-silapentane-1-sulfonic acid and 10% D₂O (v/v) for referencing, shimming, and phasing.

Cell culture

HEK293 cells stably expressing YFP-Orai1 were a generous gift from Dr. Monica Vig (Washington University, St. Louis, MO) (68). Cells were cultured in Dulbecco's modified Eagle's medium containing 10% (v/v) fetal bovine serum (Wisent), 100 μg/ml penicillin–streptomycin, and 0.4 mg/ml G418 disulfate (Thermo Fisher Scientific) and maintained at 37 °C in a 5% CO₂, 95% air humidified incubator. pCMV6 vectors containing mChSTIM1 (31, 69), and variants were transfected into cells at ~70–80% confluency using PolyJet™ transfection reagent (SignaGen Laboratories) as per the manufacturer's protocol. 4 h after transfection, GSNO was added to a final concentration of 250 μM and incubated overnight. HeLa cells were cultured and

transfected in a similar manner as the HEK cells, in the absence of G418.

Fura-2 fluorimetry

HEK293 cells were lifted off 10-cm plates by gentle pipetting and incubated with 3 μM Fura-2-AM (Alfa Aesar) in the dark at 37 °C for 45 min. The cells ($\sim 5 \times 10^6$) were subsequently washed with HEPES-buffered saline solution (HBSS; 140 mM NaCl, 4.7 mM KCl, 1.13 mM MgCl₂, 10 mM glucose, and 10 mM HEPES) and resuspended in 1.2 ml of HBSS buffer. Following the addition of 0.5 mM EGTA and an incubation period of 3 min at 22.5 °C, fluorescence using $\lambda_{\text{ex}} = 340$ and 380 nm and $\lambda_{\text{em}} = 510$ nm was measured for 900 s using a Cary Eclipse spectrofluorimeter (Varian/Agilent). Approximately 1 μM TG and 2.5 mM CaCl₂ were added to the external medium at 100 and 600 s, respectively. The data were plotted as a normalized F/F_0 ratio, where F is the emission intensity ratio from 340-nm/380-nm excitation wavelengths, and F_0 is the average F of the first 10 data points before the addition of TG.

DiBAC₄ fluorimetry

HEK293 cells were lifted off 10-cm plates by gentle pipetting and incubated with 1 μM DiBAC₄(3) (Biotium) in the dark at 37 °C for 30 min. The cells ($\sim 5 \times 10^6$) were subsequently washed with HBSS and resuspended in 1.2 ml of HBSS supplemented with 2 mM CaCl₂. After a 3-min equilibration period at 22.5 °C, fluorescence at $\lambda_{\text{ex}} = 490$ and $\lambda_{\text{em}} = 520$ nm was measured using the Cary Eclipse spectrofluorimeter. The data were plotted as F/F_0 after a straight baseline subtraction was applied, where F is the emission intensity, and F_0 is the average intensity prior to the addition of 2 μM gramicidin.

TIRF imaging

TIRF microscopy was performed on live HeLa cells that were plated on 35-mm Matsunami glass bottom (#1.5) dishes. Transfected cells were washed with HBSS supplemented with 1.5 mM CaCl₂. Imaging was performed at ambient temperature using a Leica DMI 6000B inverted microscope equipped with an HCX Plan-Apo 63 \times TIRF objective (NA 1.47), a 561-nm solid-state laser and C9100 Hamamatsu CCD camera. A 300-s time series was acquired on cells exhibiting low to moderate levels of mCherry fluorescence through a DsRed filter cube (excitation: BP 555/25; emission: BP 620/60) at a TIRF penetration depth of 110 nm. After 30 s of basal acquisition, 2 μM TG and 2 mM EGTA were added to the dish, and the time series was continued for an additional 270 s.

Western blotting

HEK293 cells were lysed using radioimmunoprecipitation assay buffer (10 mM Tris, 1 mM EDTA, 1% (v/v) Triton X-100, 0.1% (w/v) SDS, 0.1% (w/v) SDS, 140 mM NaCl, 1 mM phenylmethane sulfonyl fluoride, pH 8). 12- μg aliquots of protein were separated on a 10% (w/v) SDS-polyacrylamide gel and transferred to a nitrocellulose membrane (Bio-Rad). Specific proteins were detected using 1:1,000 rabbit anti-STIM1 (C-terminal) antibody (Sigma) and 1:2,000 rabbit anti-GAPDH antibody (Cell Signaling), followed by 1:2,000 goat anti-rabbit IR

fluorescent antibody (IRDye 680LT) (Thermo Fisher). Band densitometry was performed using ImageJ (v1.51).

Statistical analysis

Statistical analyses were performed using an unpaired t test when comparing between two independent groups, whereas one-way analysis of variance followed by Tukey's post hoc test was used to compare more than two treatment groups.

Author contributions—J. Z., Q. F., and P. B. S. conceptualization; J. Z. and P. B. S. formal analysis; J. Z., X. L., and P. B. S. investigation; J. Z., X. L., and P. B. S. methodology; J. Z. and P. B. S. writing-original draft; J. Z. and Q. F. writing-review and editing; Q. F. and P. B. S. resources; Q. F. and P. B. S. supervision; Q. F. and P. B. S. funding acquisition; Q. F. and P. B. S. project administration; P. B. S. validation; P. B. S. visualization.

Note Added in Proof—Physiologically, recent work showed that neuronal nitric oxide synthase mediates STIM1 S-nitrosylation in primary mouse cardiomyocytes (73).

References

- Berridge, M. J., Bootman, M. D., and Roderick, H. L. (2003) Calcium signalling: dynamics, homeostasis and remodelling. *Nat. Rev. Mol. Cell Biol.* **4**, 517–529 [CrossRef Medline](#)
- Hunton, D. L., Lucchesi, P. A., Pang, Y., Cheng, X., Dell'Italia, L. J., and Marchase, R. B. (2002) Capacitative calcium entry contributes to nuclear factor of activated T-cells nuclear translocation and hypertrophy in cardiomyocytes. *J. Biol. Chem.* **277**, 14266–14273 [CrossRef Medline](#)
- Collins, H. E., Zhu-Mauldin, X., Marchase, R. B., and Chatham, J. C. (2013) STIM1/Orai1-mediated SOCE: current perspectives and potential roles in cardiac function and pathology. *Am. J. Physiol. Heart Circ. Physiol.* **305**, H446–H458 [CrossRef Medline](#)
- Feske, S. (2007) Calcium signalling in lymphocyte activation and disease. *Nat. Rev. Immunol.* **7**, 690–702 [CrossRef Medline](#)
- Putney, J. W. (1986) A model for receptor-regulated calcium entry. *Cell Calcium* **7**, 1–12 [CrossRef Medline](#)
- Liou, J., Kim, M. L., Heo, W. D., Jones, J. T., Myers, J. W., Ferrell, J. E., Jr., and Meyer, T. (2005) STIM is a Ca²⁺ sensor essential for Ca²⁺-store-depletion-triggered Ca²⁺ influx. *Curr. Biol.* **15**, 1235–1241 [CrossRef Medline](#)
- Roos, J., DiGregorio, P. J., Yeromin, A. V., Ohlsen, K., Lioudyno, M., Zhang, S., Safrina, O., Kozak, J. A., Wagner, S. L., Cahalan, M. D., Velichelebi, G., and Stauderman, K. A. (2005) STIM1, an essential and conserved component of store-operated Ca²⁺ channel function. *J. Cell Biol.* **169**, 435–445 [CrossRef Medline](#)
- Zhang, S. L., Yu, Y., Roos, J., Kozak, J. A., Deerinck, T. J., Ellisman, M. H., Stauderman, K. A., and Cahalan, M. D. (2005) STIM1 is a Ca²⁺ sensor that activates CRAC channels and migrates from the Ca²⁺ store to the plasma membrane. *Nature* **437**, 902–905 [CrossRef Medline](#)
- Zhou, Y., Meraner, P., Kwon, H. T., Machnes, D., Oh-hora, M., Zimmer, J., Huang, Y., Stura, A., Rao, A., and Hogan, P. G. (2010) STIM1 gates the store-operated calcium channel ORAI1 *in vitro*. *Nat. Struct. Mol. Biol.* **17**, 112–116 [CrossRef Medline](#)
- Stathopoulos, P. B., Li, G.-Y., Plevin, M. J., Ames, J. B., and Ikura, M. (2006) Store Ca²⁺ depletion-induced oligomerization of stromal interaction molecule 1 (STIM1) via the EF-SAM region: an initiation mechanism for capacitive Ca²⁺ entry. *J. Biol. Chem.* **281**, 35855–35862 [CrossRef Medline](#)
- Liou, J., Fivaz, M., Inoue, T., and Meyer, T. (2007) Live-cell imaging reveals sequential oligomerization and local plasma membrane targeting of stromal interaction molecule 1 after Ca²⁺ store depletion. *Proc. Natl. Acad. Sci. U.S.A.* **104**, 9301–9306 [CrossRef Medline](#)
- Feske, S., Gwack, Y., Prakriya, M., Srikanth, S., Puppel, S.-H., Tanasa, B., Hogan, P. G., Lewis, R. S., Daly, M., and Rao, A. (2006) A mutation in Orai1

S-Nitrosylation inhibits STIM1 via charge sensing by EFSAM

- causes immune deficiency by abrogating CRAC channel function. *Nature* **441**, 179–185 [CrossRef Medline](#)
13. Prakriya, M., Feske, S., Gwack, Y., Srikanth, S., Rao, A., and Hogan, P. G. (2006) Orai1 is an essential pore subunit of the CRAC channel. *Nature* **443**, 230–233 [CrossRef Medline](#)
 14. Vig, M., Beck, A., Billingsley, J. M., Lis, A., Parvez, S., Peinelt, C., Koomoa, D. L., Soboloff, J., Gill, D. L., Fleig, A., Kinet, J. P., and Penner, R. (2006) CRACM1 multimers form the ion-selective pore of the CRAC channel. *Curr. Biol.* **16**, 2073–2079 [CrossRef Medline](#)
 15. Vig, M., Peinelt, C., Beck, A., Koomoa, D. L., Rabah, D., Koblan-Huberson, M., Kraft, S., Turner, H., Fleig, A., Penner, R., and Kinet, J. P. (2006) CRACM1 is a plasma membrane protein essential for store-operated Ca^{2+} entry. *Science* **312**, 1220–1223 [CrossRef Medline](#)
 16. Zhou, Y., Ramachandran, S., Oh-Hora, M., Rao, A., and Hogan, P. G. (2010) Pore architecture of the Orai1 store-operated calcium channel. *Proc. Natl. Acad. Sci. U.S.A.* **107**, 4896–4901 [CrossRef Medline](#)
 17. Frischauf, I., Muik, M., Derler, I., Bergsmann, J., Fahrner, M., Schindl, R., Groschner, K., and Romanin, C. (2009) Molecular determinants of the coupling between STIM1 and Orai channels: differential activation of Orai1–3 channels by a STIM1 coiled-coil mutant. *J. Biol. Chem.* **284**, 21696–21706 [CrossRef Medline](#)
 18. Muik, M., Fahrner, M., Derler, I., Schindl, R., Bergsmann, J., Frischauf, I., Groschner, K., and Romanin, C. (2009) A cytosolic homomerization and a modulatory domain within STIM1 C terminus determine coupling to Orai1 channels. *J. Biol. Chem.* **284**, 8421–8426 [CrossRef Medline](#)
 19. Muik, M., Fahrner, M., Schindl, R., Stathopoulos, P., Frischauf, I., Derler, I., Plenk, P., Lackner, B., Groschner, K., Ikura, M., and Romanin, C. (2011) STIM1 couples to Orai1 via an intramolecular transition into an extended conformation. *EMBO J.* **30**, 1678–1689 [CrossRef Medline](#)
 20. Park, C. Y., Hoover, P. J., Mullins, F. M., Bachhawat, P., Covington, E. D., Raunser, S., Walz, T., Garcia, K. C., Dolmetsch, R. E., and Lewis, R. S. (2009) STIM1 clusters and activates CRAC channels via direct binding of a cytosolic domain to Orai1. *Cell* **136**, 876–890 [CrossRef Medline](#)
 21. Yuan, J. P., Zeng, W., Dorwart, M. R., Choi, Y. J., Worley, P. F., and Muallem, S. (2009) SOAR and the polybasic STIM1 domains gate and regulate Orai channels. *Nat. Cell Biol.* **11**, 337–343 [CrossRef Medline](#)
 22. Covington, E. D., Wu, M. M., and Lewis, R. S. (2010) Essential role for the CRAC activation domain in store-dependent oligomerization of STIM1. *Mol. Biol. Cell* **21**, 1897–1907 [CrossRef Medline](#)
 23. Luik, R. M., Wang, B., Prakriya, M., Wu, M. M., and Lewis, R. S. (2008) Oligomerization of STIM1 couples ER calcium depletion to CRAC channel activation. *Nature* **454**, 538–542 [CrossRef Medline](#)
 24. Stathopoulos, P. B., Zheng, L., Li, G.-Y., Plevin, M. J., and Ikura, M. (2008) Structural and mechanistic insights into STIM1-mediated initiation of store-operated calcium entry. *Cell* **135**, 110–122 [CrossRef Medline](#)
 25. Stathopoulos, P. B., Zheng, L., and Ikura, M. (2009) Stromal interaction molecule (STIM) 1 and STIM2 calcium sensing regions exhibit distinct unfolding and oligomerization kinetics. *J. Biol. Chem.* **284**, 728–732 [CrossRef Medline](#)
 26. Zhou, Y., Mancarella, S., Wang, Y., Yue, C., Ritchie, M., Gill, D. L., and Soboloff, J. (2009) The short N-terminal domains of STIM1 and STIM2 control the activation kinetics of Orai1 channels. *J. Biol. Chem.* **284**, 19164–19168 [CrossRef Medline](#)
 27. Hawkins, B. J., Irrinki, K. M., Mallilankaraman, K., Lien, Y.-C., Wang, Y., Bhanumathy, C. D., Subbiah, R., Ritchie, M. F., Soboloff, J., Baba, Y., Kurosaki, T., Joseph, S. K., Gill, D. L., and Madesh, M. (2010) S-glutathionylation activates STIM1 and alters mitochondrial homeostasis. *J. Cell Biol.* **190**, 391–405 [CrossRef Medline](#)
 28. Aracena-Parks, P., Goonasekera, S. A., Gilman, C. P., Dirksen, R. T., Hidalgo, C., and Hamilton, S. L. (2006) Identification of cysteines involved in S-nitrosylation, S-glutathionylation, and oxidation to disulfides in ryanodine receptor type 1. *J. Biol. Chem.* **281**, 40354–40368 [CrossRef Medline](#)
 29. Giustarini, D., Milzani, A., Aldini, G., Carini, M., Rossi, R., and Dalle-Donne, I. (2005) S-Nitrosation versus S-glutathionylation of protein sulfhydryl groups by S-nitrosoglutathione. *Antioxid. Redox. Signal.* **7**, 930–939 [CrossRef Medline](#)
 30. Gould, N., Doulias, P.-T., Tenopoulou, M., Raju, K., and Ischiropoulos, H. (2013) Regulation of protein function and signaling by reversible cysteine S-nitrosylation. *J. Biol. Chem.* **288**, 26473–26479 [CrossRef Medline](#)
 31. Luik, R. M., Wu, M. M., Buchanan, J., and Lewis, R. S. (2006) The elementary unit of store-operated Ca^{2+} entry: local activation of CRAC channels by STIM1 at ER-plasma membrane junctions. *J. Cell Biol.* **174**, 815–825 [CrossRef Medline](#)
 32. Wu, M. M., Buchanan, J., Luik, R. M., and Lewis, R. S. (2006) Ca^{2+} store depletion causes STIM1 to accumulate in ER regions closely associated with the plasma membrane. *J. Cell Biol.* **174**, 803–813 [CrossRef Medline](#)
 33. Pace, C. N. (1986) Determination and analysis of urea and guanidine hydrochloride denaturation curves. *Methods Enzymol.* **131**, 266–280 [CrossRef Medline](#)
 34. Stryer, L. (1965) The interaction of a naphthalene dye with apomyoglobin and apohemoglobin: a fluorescent probe of non-polar binding sites. *J. Mol. Biol.* **13**, 482–495 [CrossRef Medline](#)
 35. Li, Y., Lubchenko, V., and Vekilov, P. G. (2011) The use of dynamic light scattering and brownian microscopy to characterize protein aggregation. *Rev. Sci. Instrum.* **82**, 053106 [CrossRef Medline](#)
 36. Clore, G. M., and Iwahara, J. (2009) Theory, practice, and applications of paramagnetic relaxation enhancement for the characterization of transient low-population states of biological macromolecules and their complexes. *Chem. Rev.* **109**, 4108–4139 [CrossRef Medline](#)
 37. Okamoto, S., Nakamura, T., Cieplak, P., Chan, S. F., Kalashnikova, E., Liao, L., Saleem, S., Han, X., Clemente, A., Nutter, A., Sances, S., Brechtel, C., Haus, D., Haun, F., Sanz-Blasco, S., et al. (2014) S-Nitrosylation-mediated redox transcriptional switch modulates neurogenesis and neuronal cell death. *Cell Rep.* **8**, 217–228 [CrossRef Medline](#)
 38. Mercer, J. C., Dehaven, W. I., Smyth, J. T., Wedel, B., Boyles, R. R., Bird, G. S., and Putney, J. W. (2006) Large store-operated calcium selective currents due to co-expression of Orai1 or Orai2 with the intracellular calcium sensor, Stim1. *J. Biol. Chem.* **281**, 24979–24990 [CrossRef Medline](#)
 39. Feng, J. H., Jing, F. B., Fang, H., Gu, L. C., and Xu, W. F. (2011) Expression, purification, and S-nitrosylation of recombinant histone deacetylase 8 in *Escherichia coli*. *Biosci. Trends* **5**, 17–22 [CrossRef Medline](#)
 40. Hao, G., Xie, L., and Gross, S. S. (2004) Argininosuccinate synthetase is reversibly inactivated by S-nitrosylation *in vitro* and *in vivo*. *J. Biol. Chem.* **279**, 36192–36200 [CrossRef Medline](#)
 41. Liu, L., Enright, E., Sun, P., Tsai, S. Y., Mehta, P., Beckman, D. L., and Terrian, D. M. (2002) Inactivation of annexin II tetramer by S-nitrosoglutathione. *Eur. J. Biochem.* **269**, 4277–4286 [CrossRef Medline](#)
 42. Bocedi, A., Gradoni, L., Menegatti, E., and Ascenzi, P. (2004) Kinetics of parasite cysteine proteinase inactivation by NO-donors. *Biochem. Biophys. Res. Commun.* **315**, 710–718 [CrossRef Medline](#)
 43. Broniowska, K. A., Diers, A. R., and Hogg, N. (2013) S-Nitrosoglutathione. *Biochim. Biophys. Acta* **1830**, 3173–3181 [CrossRef Medline](#)
 44. Martínez-Ruiz, A., Araújo, I. M., Izquierdo-Álvarez, A., Hernansanz-Agustín, P., Lamas, S., and Serrador, J. M. (2013) Specificity in S-nitrosylation: a short-range mechanism for NO signaling? *Antioxid. Redox. Signal.* **19**, 1220–1235 [CrossRef Medline](#)
 45. Sun, J., Steenbergen, C., and Murphy, E. (2006) S-nitrosylation: NO-related redox signaling to protect against oxidative stress. *Antioxid. Redox. Signal.* **8**, 1693–1705 [CrossRef Medline](#)
 46. Martínez-Ruiz, A., and Lamas, S. (2007) Signalling by NO-induced protein S-nitrosylation and S-glutathionylation: convergences and divergences. *Cardiovasc. Res.* **75**, 220–228 [CrossRef Medline](#)
 47. Haldar, S. M., and Stamler, J. S. (2013) S-nitrosylation: integrator of cardiovascular performance and oxygen delivery. *J. Clin. Invest.* **123**, 101–110 [CrossRef Medline](#)
 48. Hess, D. T., and Stamler, J. S. (2012) Regulation by S-nitrosylation of protein post-translational modification. *J. Biol. Chem.* **287**, 4411–4418 [CrossRef Medline](#)
 49. Barnett, S. D., and Buxton, I. L. O. (2017) The role of S-nitrosoglutathione reductase (GSNOR) in human disease and therapy. *Crit. Rev. Biochem. Mol. Biol.* **52**, 340–354 [CrossRef Medline](#)
 50. Prins, D., Groenendyk, J., Touret, N., and Michalak, M. (2011) Modulation of STIM1 and capacitative Ca^{2+} entry by the endoplasmic reticulum lu-

- minal oxidoreductase ERp57. *EMBO Rep.* **12**, 1182–1188 [CrossRef Medline](#)
51. Cai, Z., Lu, Q., Ding, Y., Wang, Q., Xiao, L., Song, P., and Zou, M. H. (2015) Endothelial nitric oxide synthase-derived nitric oxide prevents dihydrofolate reductase degradation via promoting S-nitrosylation. *Arterioscler. Thromb. Vasc. Biol.* **35**, 2366–2373 [CrossRef Medline](#)
 52. Kohr, M. J., Evangelista, A. M., Ferlito, M., Steenbergen, C., and Murphy, E. (2014) S-Nitrosylation of TRIM72 at cysteine 144 is critical for protection against oxidation-induced protein degradation and cell death. *J. Mol. Cell Cardiol.* **69**, 67–74 [CrossRef Medline](#)
 53. Takahashi, H., Shin, Y., Cho, S. J., Zago, W. M., Nakamura, T., Gu, Z., Ma, Y., Furukawa, H., Liddington, R., Zhang, D., Tong, G., Chen, H. S., and Lipton, S. A. (2007) Hypoxia enhances S-nitrosylation-mediated NMDA receptor inhibition via a thiol oxygen sensor motif. *Neuron* **53**, 53–64 [CrossRef Medline](#)
 54. Renganathan, M., Cummins, T. R., and Waxman, S. G. (2002) Nitric oxide blocks fast, slow, and persistent Na⁺ channels in C-type DRG neurons by S-nitrosylation. *J. Neurophysiol.* **87**, 761–775 [CrossRef Medline](#)
 55. Li, F., Sonveaux, P., Rabbani, Z. N., Liu, S., Yan, B., Huang, Q., Vujaskovic, Z., Dewhirst, M. W., and Li, C. Y. (2007) Regulation of HIF-1 α stability through S-nitrosylation. *Mol. Cell* **26**, 63–74 [CrossRef Medline](#)
 56. Kumar, R., Jangir, D. K., Verma, G., Shekhar, S., Hanpude, P., Kumar, S., Kumari, R., Singh, N., Sarovar Bhavesh, N., Ranjan Jana, N., and Kanti Maiti, T. (2017) S-Nitrosylation of UCHL1 induces its structural instability and promotes α -synuclein aggregation. *Sci. Rep.* **7**, 44558 [CrossRef Medline](#)
 57. Qu, J., Liu, G. H., Wu, K., Han, P., Wang, P., Li, J., Zhang, X., and Chen, C. (2007) Nitric oxide destabilizes Pias3 and regulates sumoylation. *PLoS One* **2**, e1085 [CrossRef Medline](#)
 58. Albertos, P., Romero-Puertas, M. C., Tatematsu, K., Mateos, I., Sánchez-Vicente, I., Nambara, E., and Lorenzo, O. (2015) S-Nitrosylation triggers ABI5 degradation to promote seed germination and seedling growth. *Nat. Commun.* **6**, 8669 [CrossRef Medline](#)
 59. Guo, C. J., Atochina-Vasserman, E. N., Abramova, E., Foley, J. P., Zaman, A., Crouch, E., Beers, M. F., Savani, R. C., and Gow, A. J. (2008) S-Nitrosylation of surfactant protein-D controls inflammatory function. *PLoS Biol.* **6**, e266 [CrossRef Medline](#)
 60. Eichmann, C., Tzitzilonis, C., Nakamura, T., Kwiatkowski, W., Maslennikov, I., Choe, S., Lipton, S. A., and Riek, R. (2016) S-Nitrosylation induces structural and dynamical changes in a rhodanese family protein. *J. Mol. Biol.* **428**, 3737–3751 [CrossRef Medline](#)
 61. Ma, G., Wei, M., He, L., Liu, C., Wu, B., Zhang, S. L., Jing, J., Liang, X., Senes, A., Tan, P., Li, S., Sun, A., Bi, Y., Zhong, L., Si, H., et al. (2015) Inside-out Ca²⁺ signalling prompted by STIM1 conformational switch. *Nat. Commun.* **6**, 7826 [CrossRef Medline](#)
 62. Zhou, Y., Srinivasan, P., Razavi, S., Seymour, S., Meraner, P., Gudlur, A., Stathopoulos, P. B., Ikura, M., Rao, A., and Hogan, P. G. (2013) Initial activation of STIM1, the regulator of store-operated calcium entry. *Nat. Struct. Mol. Biol.* **20**, 973–981 [CrossRef Medline](#)
 63. Zheng, L., Stathopoulos, P. B., Schindl, R., Li, G. Y., Romanin, C., and Ikura, M. (2011) Auto-inhibitory role of the EF-SAM domain of STIM proteins in store-operated calcium entry. *Proc. Natl. Acad. Sci. U.S.A.* **108**, 1337–1342 [CrossRef Medline](#)
 64. Choi, Y. J., Zhao, Y., Bhattacharya, M., and Stathopoulos, P. B. (2017) Structural perturbations induced by Asn131 and Asn171 glycosylation converge within the EFSAM core and enhance stromal interaction molecule-1 mediated store operated calcium entry. *Biochim. Biophys. Acta* **1864**, 1054–1063 [CrossRef Medline](#)
 65. Hart, T. W. (1985) Some observations concerning the S-nitroso and S-phenylsulphonyl derivatives of L-cysteine and glutathione. *Tetrahedron Lett.* **26**, 2013–2016 [CrossRef](#)
 66. Farrow, N. A., Muhandiram, R., Singer, A. U., Pascal, S. M., Kay, C. M., Gish, G., Shoelson, S. E., Pawson, T., Forman-Kay, J. D., and Kay, L. E. (1994) Backbone dynamics of a free and phosphopeptide-complexed Src homology 2 domain studied by ¹⁵N NMR relaxation. *Biochemistry* **33**, 5984–6003 [CrossRef Medline](#)
 67. Kay, L. E., Keifer, P., and Saarienen, T. (1992) Pure absorption gradient enhanced heteronuclear single quantum correlation spectroscopy with improved sensitivity. *J. Am. Chem. Soc.* **114**, 10663–10665 [CrossRef](#)
 68. Miao, Y., Miner, C., Zhang, L., Hanson, P. I., Dani, A., and Vig, M. (2013) An essential and NSF independent role for α -SNAP in store-operated calcium entry. *Elife* **2**, e00802 [Medline](#)
 69. Stathopoulos, P. B., Schindl, R., Fahrner, M., Zheng, L., Gasmi-Seabrook, G. M., Muik, M., Romanin, C., and Ikura, M. (2013) STIM1/Orai1 coiled-coil interplay in the regulation of store-operated calcium entry. *Nat. Commun.* **4**, 2963 [Medline](#)
 70. Sievers, F., and Higgins, D. G. (2014) Clustal omega. *Curr. Prot. Bioinformatics* **48**, 3.13.1–3.13.16 [Medline](#)
 71. Baker, N. A., Sept, D., Joseph, S., Holst, M. J., and McCammon, J. A. (2001) Electrostatics of nanosystems: application to microtubules and the ribosome. *Proc. Natl. Acad. Sci. U.S.A.* **98**, 10037–10041 [CrossRef Medline](#)
 72. Dolinsky, T. J., Czodrowski, P., Li, H., Nielsen, J. E., Jensen, J. H., Klebe, G., and Baker, N. A. (2007) PDB2PQR: expanding and upgrading automated preparation of biomolecular structures for molecular simulations. *Nucleic Acids Res.* **35**, W522–W525 [CrossRef Medline](#)
 73. Gui, L., Zhu, J., Lu, X., Sims, S. M., Lu, W. Y., Stathopoulos, P. B., and Feng, Q. (2018) S-Nitrosylation of STIM1 by neuronal nitric oxide synthase inhibits store-operated Ca²⁺ entry. *J. Mol. Biol.* [CrossRef Medline](#)

A charge-sensing region in the stromal interaction molecule 1 luminal domain confers stabilization-mediated inhibition of SOCE in response to *S*-nitrosylation

Jinhui Zhu, Xiangru Lu, Qingping Feng and Peter B. Stathopoulos

J. Biol. Chem. 2018, 293:8900-8911.

doi: 10.1074/jbc.RA117.000503 originally published online April 16, 2018

Access the most updated version of this article at doi: [10.1074/jbc.RA117.000503](https://doi.org/10.1074/jbc.RA117.000503)

Alerts:

- [When this article is cited](#)
- [When a correction for this article is posted](#)

[Click here](#) to choose from all of JBC's e-mail alerts

This article cites 73 references, 23 of which can be accessed free at <http://www.jbc.org/content/293/23/8900.full.html#ref-list-1>

Supplementary Table 1. Thermodynamic stability parameters for STIM1 23-213 variants with and without GSNO.

STIM1 23-213 protein	-GSNO ^a			+GSNO ^b			$\Delta\Delta G^f$ (kcal mol ⁻¹)
	$\Delta G_{H_2O}^c$ (kcal mol ⁻¹)	C_{mid}^d (M)	m -value ^e (kcal mol ⁻¹ M ⁻¹)	$\Delta G_{H_2O}^c$ (kcal mol ⁻¹)	C_{mid}^d (M)	m -value ^e (kcal mol ⁻¹ M ⁻¹)	
<i>Ca²⁺-loaded</i>							
WT	5.91 ± 0.03	3.09 ± 0.02	1.91 ± 0.07	7.87 ± 0.15	3.29 ± 0.06	2.39 ± 0.06	+1.96
<i>Ca²⁺-depleted</i>							
WT	1.73 ± 0.01	1.33 ± 0.01	1.30 ± 0.04	3.23 ± 0.06	1.76 ± 0.03	1.83 ± 0.06	+1.50
C49S/C56S	1.75 ± 0.03	1.12 ± 0.02	1.55 ± 0.11	1.45 ± 0.06	1.15 ± 0.05	1.28 ± 0.07	-0.30
W121E/K122E	3.88 ± 0.02	2.33 ± 0.01	1.67 ± 0.09	4.25 ± 0.06	2.87 ± 0.03	1.54 ± 0.18	+0.37

^aData acquired in the presence of 1 mM DTT (*i.e.* absence of GSNO).

^bData acquired in the presence of 1 mM GSNO.

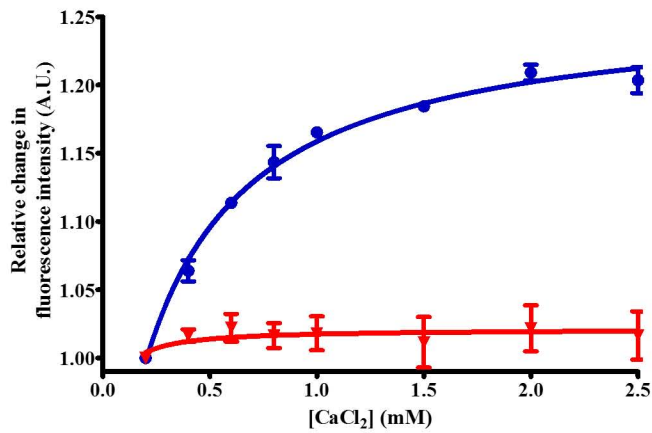
^cGibbs free energy of unfolding; data fit to a two-state equilibrium unfolding model; globally fit to n=3 separate denaturation curves.

^dMidpoint of chemical denaturation; calculated as $\Delta G_{H_2O}/m$.

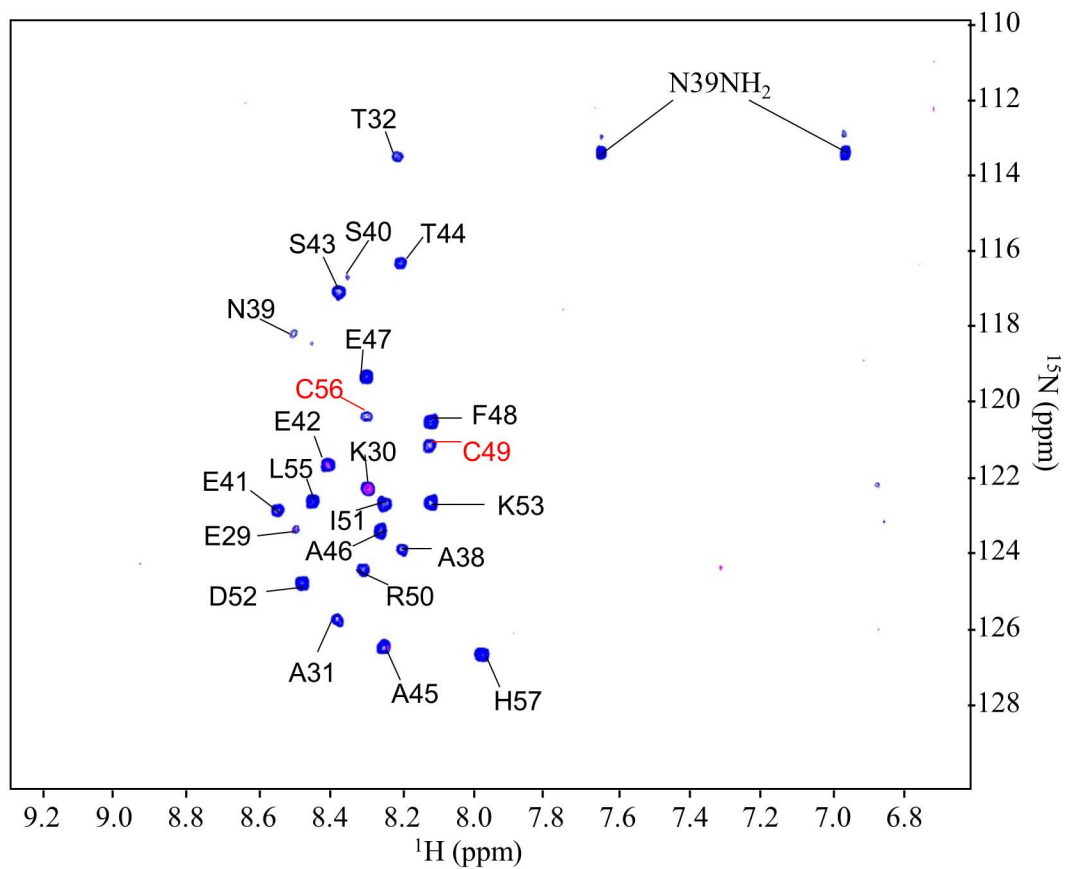
^eDenaturant dependence of the unfolding; globally fit to n=3 separate denaturation curves.

^f $\Delta G_{H_2O(+GSNO)} - \Delta G_{H_2O(-GSNO)}$.

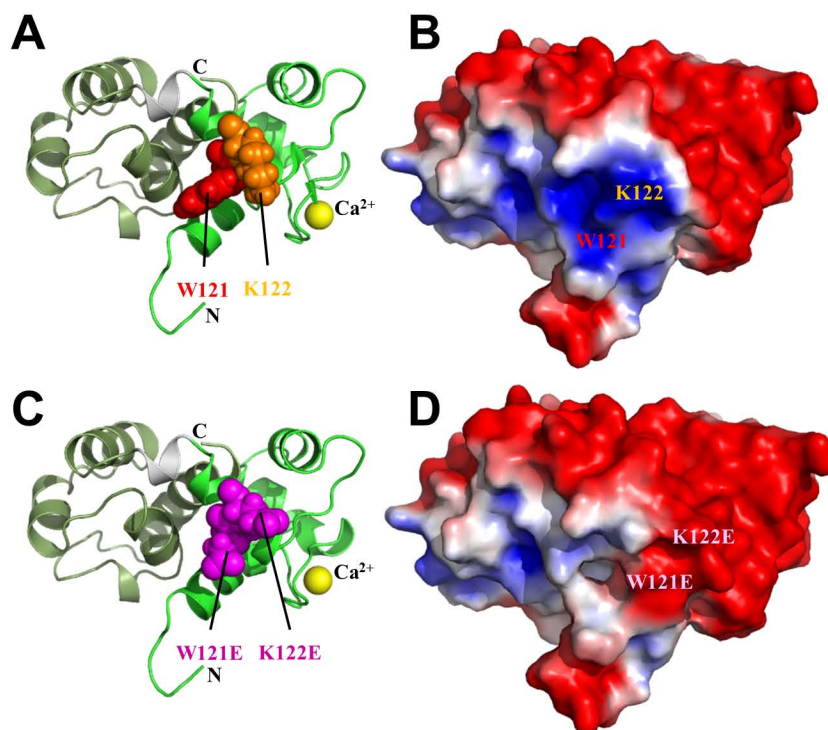
Errors (±) in ΔG_{H_2O} and C_{mid} are SEM, while errors (±) in m -value are standard errors outputted from the global fits of n=3 separate denaturation curves for each group.



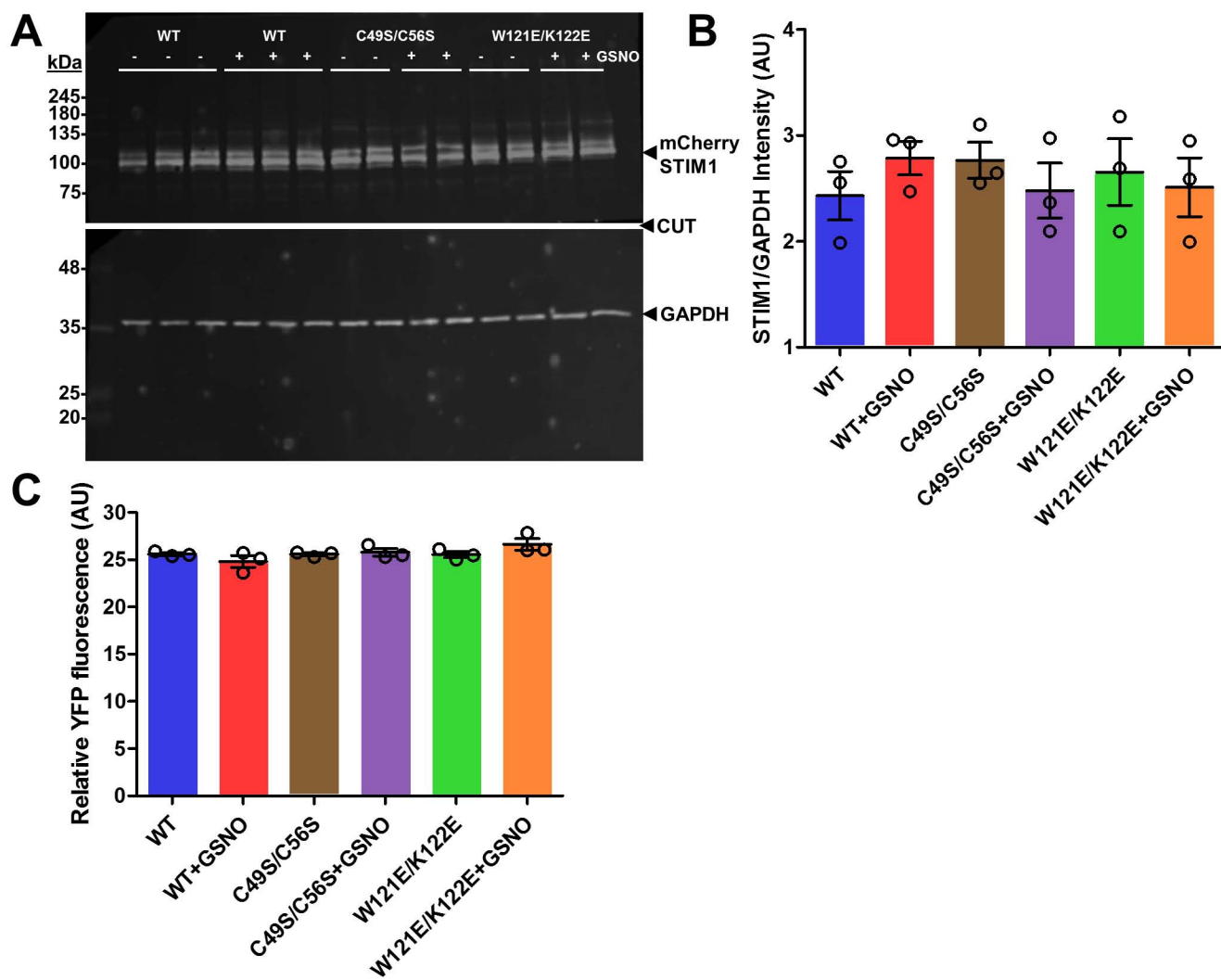
Supplementary Fig. 1. Ca²⁺ binding to WT STIM1 23-213 with and without GSNO donors, indirectly monitored by intrinsic fluorescence changes. The solid lines through the data represent the non-linear least squares fit of the data to a one site binding model which takes into account protein concentration. The fitted apparent equilibrium dissociation constants (K_d) for the WT STIM1 23-213 protein in 1 mM DTT was 0.30 ± 0.04 mM. Due to the miniscule change in intrinsic fluorescence for the protein in the presence of GSNO, the K_d could not be reliably determined in the presence of the NO donor. Data are means \pm SEM of $n=3$ separate experiments.



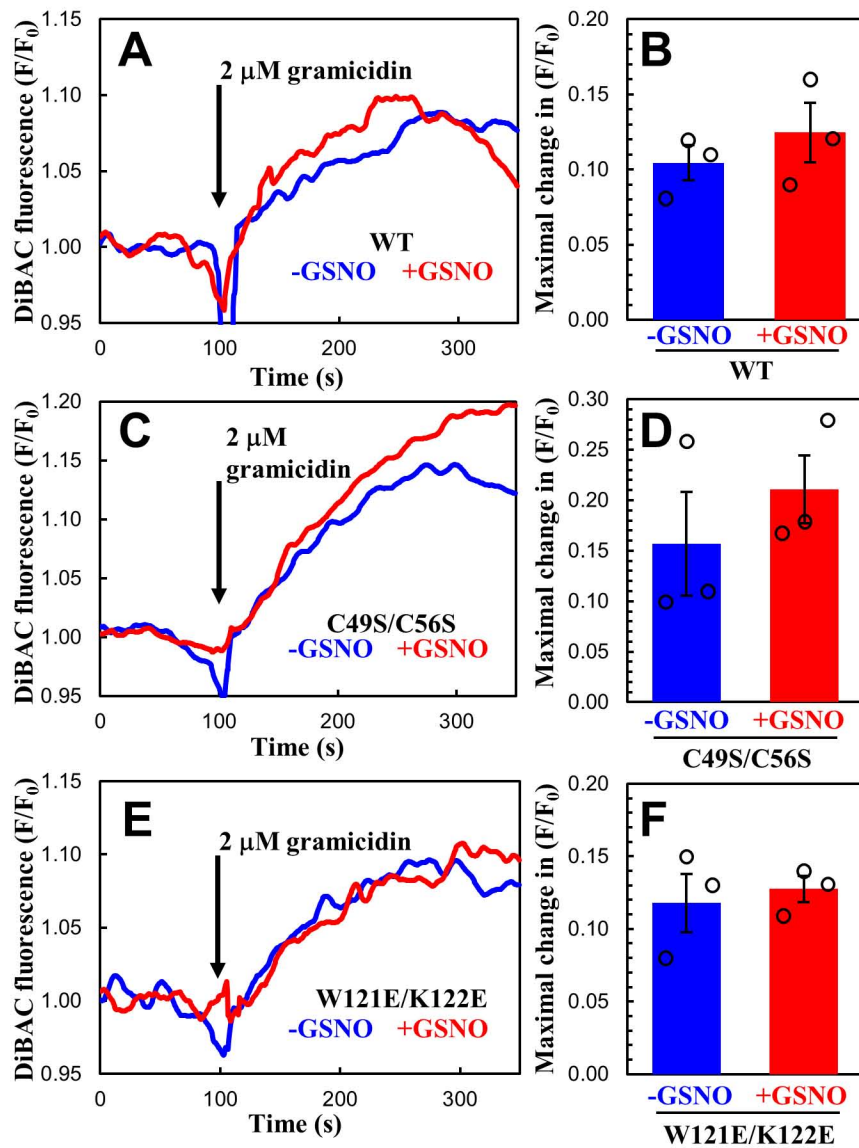
Supplementary Fig. 2. ^1H - ^{15}N -HSQC spectra of nitroxide-tagged STIM1 24-57. ^1H - ^{15}N -HSQC spectrum of nitroxide spin-tagged and ^{15}N -labeled STIM1 24-57 before (magenta) and after the addition of 15 mM DTT (blue). The severe broadening observed for most of the peaks in the absence of DTT is consistent with efficient spin tagging at the Cys49 and Cys56 sites; further, the recovery of the peak intensities after DTT treatment validates our removal methodology for acquisition of baseline intensities.



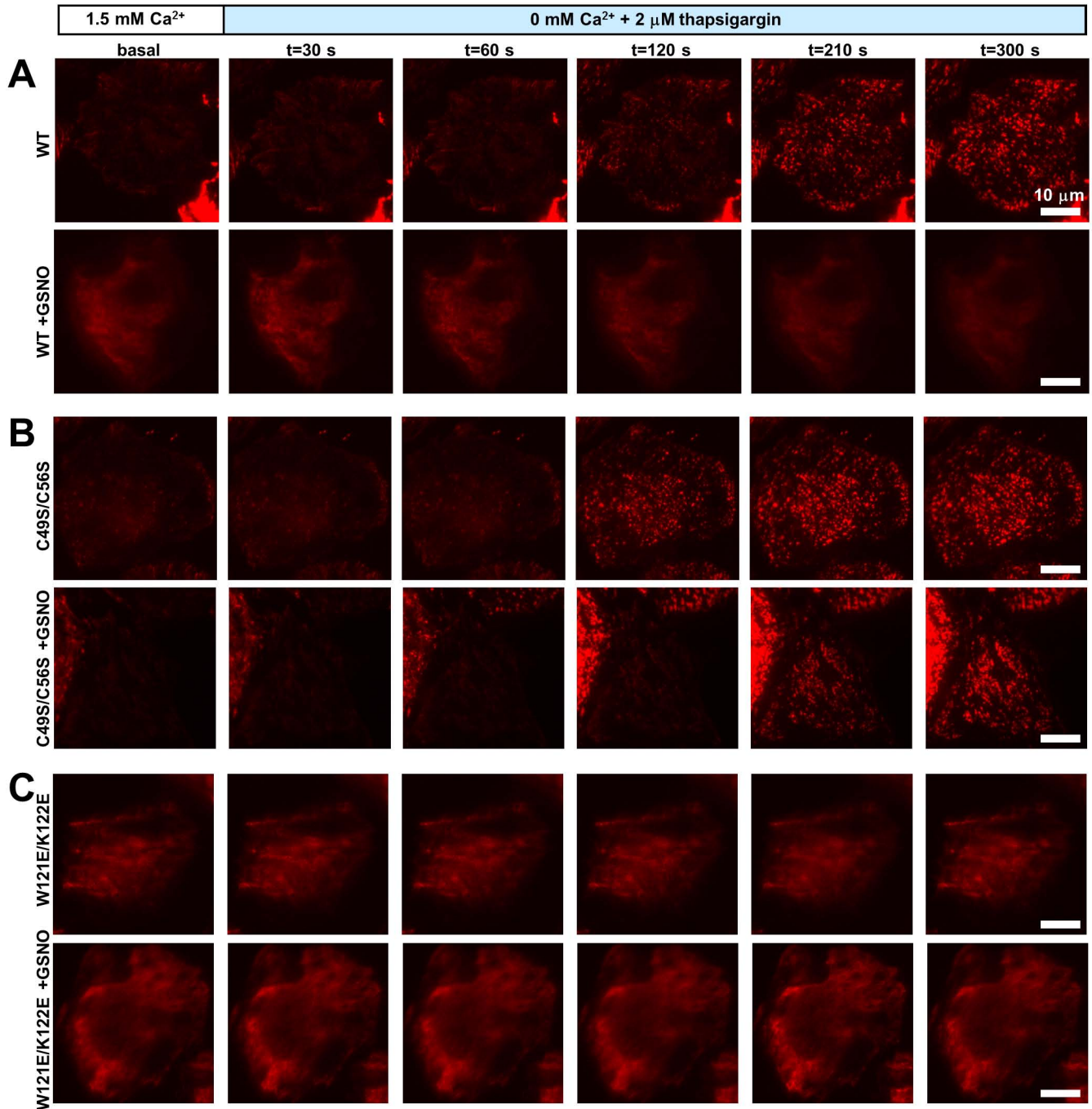
Supplementary Fig. 3. Location of W121 and K122 relative to the backbone structure and consequence of the W121E/K122E mutation on the electrostatic potential of Ca²⁺-loaded STIM1 EFSAM. *A.* Ribbon representation of the Ca²⁺-loaded STIM1 EFSAM structure highlighting the location of W121 (red spacefill) and K122 (orange spacefill). *B.* Electrostatic surface potential of Ca²⁺-loaded STIM1 EFSAM. The locations of the W121 and K122 residues relative to the distinct electropositive patch are shown. *C.* Ribbon representation of the Ca²⁺-loaded STIM1 EFSAM structure highlighting the location of W121E and K122E mutant side chains (magenta spacefill) indicating no major steric clashes. *D.* Electrostatic surface potential of Ca²⁺-loaded STIM1 EFSAM. The W121E/K122E mutation results in a major disruption in the electropositive patch and extends the primary electronegative surface potential into the EF-hand domain at the W121E and K122E location. In (*A*) and (*C*), the EF-hand (light green) and SAM domain (dark green) are connected by a short linker region (grey). The Ca²⁺ atom is shown as a yellow sphere. In (*B*) and (*D*), the surface potential is shown as a gradient between +2 and -2 kT/e determined using the APBS and PDB2PQR tools (71,72). Structure images were rendered using PyMOL (The PyMOL Molecular Graphics System, Version 1.7 Schrödinger, LLC).



Supplementary Fig. 4. Effects of GSNO on mChSTIM1 protein levels in HEK293 cells stably expressing YFP-Orail. *A*. Representative western blots of transient mChSTIM1 (~101 kDa) and endogenous GAPDH (~36 kDa) protein expression levels. *B*. Western blot mChSTIM1 band intensity normalized relative to GAPDH. *C*. Relative YFP fluorescence of cell suspensions ($\lambda_{\text{ex}} = 490 \text{ nm}$ and $\lambda_{\text{em}} = 500 - 600 \text{ nm}$) normalized to cell density ($F_{\text{max}}/F_{\text{min}}$). Data in (*B*) and (*C*) are means \pm SEM of $n=3$ separate transfections for each group.



Supplementary Fig. 5. Effects of GSNO on HEK293 cell membrane potential. Mean DiBAC₄(3) fluorescence traces (10 s moving average) of HEK293 cells stably expressing YFP-Orai1 and transiently expressing (A) WT, (C) C49S/C56S and (E) W121E/K122E mChSTIM1 showing relative changes in membrane potential after monovalent ion permeabilization with 2 μM gramicidin (black arrows). Maximal relative DiBAC₄(3) signal change after gramicidin-induced depolarization for (B) WT, (D) C49S/C56S and (F) W121E/K122E mChSTIM1 expressing cells. Data in (B), (D) and (F) are means ± SEM of n=3 separate transfections for each group.



Supplementary Fig. 6. GSNO sensitivity of mChSTIM1 puncta formation in live HeLa cells. Time series of TIRF-visualized puncta formation after 2 μM TG addition to HeLa cells expressing (A) WT, (B) C49S/C56S and (C) W121E/K122E mChSTIM1. The time after the addition of TG is shown above the images acquired at ambient temperature. A 10 μm bar (white) is shown in the final image of each series for scale. Data in (A) – (C) are representative of n=3 separate transfections for each series.